FERMILAB-PUB-12-563-AD-AE-CD-TD

Large scale distribution of arrival directions of cosmic rays detected above 10^{18} eV at the Pierre Auger observatory

The Pierre Auger Collaboration

Av. San Martín Norte 306, 5613 Malargüe, Mendoza, Argentina; www.auger.org

Received ______________________; accepted ______________________

Operated by Fermi Research Alliance, LLC under Contract No. De-AC02-07CH11359 with the United States Department of Energy.

ABSTRACT

A thorough search for large scale anisotropies in the distribution of arrival directions of cosmic rays detected above 10^{18} eV at the Pierre Auger Observatory is presented. This search is performed in several energy ranges in terms of dipoles and quadrupoles as a function of both the declination and the right ascension. Within the systematic uncertainties, no significant deviation from isotropy is revealed. Assuming that the eventual anisotropic component of the angular distribution of cosmic rays is dominated by dipole and quadrupole moments in this energy range, upper limits on dipole and quadrupole amplitudes are derived. These upper limits allow us to challenge an origin of cosmic rays above 10^{18} eV from stationary galactic sources densely distributed in the galactic disk and emitting predominantly light particles in all directions.

Subject headings: Ultra-High Energy Cosmic Rays; Pierre Auger Observatory; Large Scale Anisotropies

The Pierre Auger Collaboration

P. Abreu[63], M. Aglietta[51], M. Ahlers[94], E.J. Ahn[81], I.F.M. Albuquerque[15], D. Allard[29], I. Allekotte[1], J. Allen[85], P. Allison[87], A. Almela[11, 7], J. Alvarez Castillo[56], J. Alvarez-Muñiz[73], R. Alves Batista[16], M. Ambrosio[45], A. Aminaei[57], L. Anchordoqui[95], S. Andringa[63], T. Antiči’c[23], C. Aramo[45], E. Arganda[4, 70], F. Arqueros[70], H. Asorey[1], P. Assis[63], J. Aublin[31], M. Ave[37], M. Avenier[32], G. Avila[10], A.M. Badescu[66], M. Balzer[36], K.B. Barber[12], A.F. Barbosa[13 ‡], R. Bardenet[30], S.L.C. Barroso[18], B. Baughman[87 f], J. Bäuml[35], C. Baus[37], J.J. Beatty[87], K.H. Becker[34], A. Bellétoile[33], J.A. Bellido[12], S. BenZvi[94], C. Berat[32], X. Bertou[1], P.L. Biermann[38], P. Billoir[31], F. Blanco[70], M. Blanco[31, 71], C. Bleve[34], H. Blümer[37, 35], M. Boháčová[25], D. Boncioli[46], C. Bonifazi[21, 31], R. Bonino[51], N. Borodai[61], J. Brack[79], I. Brancus[64], P. Brogueira[63], W.C. Brown[80], R. Bruijn[75 i], P. Buchholz[41], A. Bueno[72], L. Buroker[95], R.E. Burton[77], K.S. Caballero-Mora[88], B. Caccianiga[44], L. Caramete[38], R. Caruso[47], A. Castellina[51], O. Catalano[50], G. Cataldi[49], L. Cazon[63], R. Cester[48], J. Chauvin[32], S.H. Cheng[88], A. Chiavassa[51], J.A. Chinellato[16], J. Chirinos Diaz[84], J. Chudoba[25], M. Cilmo[45], R.W. Clay[12], G. Cocciolo[49], L. Collica[44], M.R. Coluccia[49], R. Conceição[63], F. Contreras[9], H. Cook[75], M.J. Cooper[12], J. Coppens[57, 59], A. Cordier[30], S. Coutu[88], C.E. Covault[77], A. Creusot[29], A. Criss[88], J. Cronin[90], A. Curutiu[38], S. Dagoret-Campagne[30], R. Dallier[33], B. Daniel[16], S. Dasso[5, 3], K. Daumiller[35], B.R. Dawson[12], R.M. de Almeida[22], M. De Domenico[47], C. De Donato[56], S.J. de Jong[57, 59], G. De La Vega[8], W.J.M. de Mello Junior[16], J.R.T. de Mello Neto[21], I. De Mitri[49], V. de Souza[14], K.D. de Vries[58], L. del Peral[71], M. del Río[46, 9], O. Deligny[28], H. Dembinski[37], N. Dhital[84], C. Di Giulio[46, 43], M.L. Díaz Castro[13], P.N. Diep[96], F. Diogo[63], C. Dobrigkeit [16], W. Docters[58], J.C. D’Olivo[56], P.N. Dong[96, 28], A. Dorofeev[79], J.C. dos Anjos[13], M.T. Dova[4], D. D’Urso[45], I. Dutan[38], J. Ebr[25], R. Engel[35], M. Erdmann[39], C.O. Escobar[81, 16], J. Espadanal[63], A. Etchegoyen[7, 11], P. Facal San Luis[90], H. Falcke[57, 60, 59], K. Fang[90], G. Farrar[85], A.C. Fauth[16], N. Fazzini[81], A.P. Ferguson[77], B. Fick[84], J.M. Figueira[7], A. Filevich[7], A. Filipčič[67, 68], S. Fliescher[39], C.E. Fracchiolla[79], E.D. Fraenkel[58], O. Fratu[66], U. Fröhlich[41], B. Fuchs[37], R. Gaior[31], R.F. Gamarra[7], S. Gambetta[42], B. García[8], S.T. Garcia Roca[73], D. Garcia-Gamez[30], D. Garcia-Pinto[70], G. Garilli[47], A. Gascon Bravo[72], H. Gemmeke[36], P.L. Ghia[31], M. Giller[62], J. Gitto[8], H. Glass[81], M.S. Gold[93], G. Golup[1], F. Gomez Albarracin[4], M. Gómez Berisso[1], P.F. Gómez Vitale[10], P. Gonçalves[63], J.G. Gonzalez[35], B. Gookin[79], A. Gorgi[51], P. Gouffon[15], E. Grashorn[87], S. Grebe[57, 59], N. Griffith[87], A.F. Grillo[52], Y. Guardincerri[3], F. Guarino[45], G.P. Guedes[17], P. Hansen[4],

D. Harari[1], T.A. Harrison[12], J.L. Harton[79], A. Haungs[35], T. Hebbeker[39], D. Heck[35], A.E. Herve[12], G.C. Hill[12], C. Hojvat[81], N. Hollon[90], V.C. Holmes[12], P. Homola[61], J.R. Hörandel[57, 59], P. Horvath[26], M. Hrabovský[26, 25], D. Huber[37], T. Huege[35], A. Insolia[47], F. Ionita[90], A. Italiano[47], S. Jansen[57, 59], C. Jarne[4], S. Jiraskova[57], M. Josebachuili[7], K. Kadija[23], K.H. Kampert[34], P. Karhan[24], P. Kasper[81], I. Katkov[37], B. Kégl[30], B. Keilhauer[35], A. Keivani[83], J.L. Kelley[57], E. Kemp[16], R.M. Kieckhafer[84], H.O. Klages[35], M. Kleifges[36], J. Kleinfeller[9, 35], J. Knapp[75], D.-H. Koang[32], K. Kotera[90], N. Krohm[34], O. Krömer[36], D. Kruppke-Hansen[34], D. Kuempel[39, 41], J.K. Kulbartz[40], N. Kunka[36], G. La Rosa[50], C. Lachaud[29], D. LaHurd[77], L. Latronico[51], R. Lauer[93], P. Lautridou[33], S. Le Coz[32], M.S.A.B. Leão[20], D. Lebrun[32], P. Lebrun[81], M.A. Leigui de Oliveira[20], A. Letessier-Selvon[31], I. Lhenry-Yvon[28], K. Link[37], R. López[53], A. Lopez Agüera[73], K. Louedec[32, 30], J. Lozano Bahilo[72], L. Lu[75], A. Lucero[7], M. Ludwig[37], H. Lyberis[21, 28], M.C. Maccarone[50], C. Macolino[31], S. Maldera[51], J. Maller[33], D. Mandat[25], P. Mantsch[81], A.G. Mariazzi[4], J. Marin[9, 51], V. Marin[33], I.C. Maris[31], H.R. Marquez Falcon[55], G. Marsella[49], D. Martello[49], L. Martin[33], H. Martinez[54], O. Martínez Bravo[53], D. Martraire[28], J.J. Masías Meza[3], H.J. Mathes[35], J. Matthews[83], J.A.J. Matthews[93], G. Matthiae[46], D. Maurel[35], D. Maurizio[13, 48], P.O. Mazur[81], G. Medina-Tanco[56], M. Melissas[37], D. Melo[7], E. Menichetti[48], A. Menshikov[36], P. Mertsch[74], S. Messina[58], C. Meurer[39], R. Meyhandan[91], S. Mi'canovi'c[23], M.I. Micheletti[6], I.A. Minaya[70], L. Miramonti[44], L. Molina-Bueno[72], S. Mollerach[1], M. Monasor[90], D. Monnier Ragaigne[30], F. Montanet[32], B. Morales[56], C. Morello[51], E. Moreno[53], J.C. Moreno[4], M. Mostafá[79], C.A. Moura[20], M.A. Muller[16], G. Müller[39], M. Münchmeyer[31], R. Mussa[48], G. Navarra[51 ‡], J.L. Navarro[72], S. Navas[72], P. Necesal[25], L. Nellen[56], A. Nelles[57, 59], J. Neuser[34], P.T. Nhung[96], M. Niechciol[41], L. Niemietz[34], N. Nierstenhoefer[34], D. Nitz[84], D. Nosek[24], L. Nožka[25], J. Oehlschläger[35], A. Olinto[90], M. Ortiz[70], N. Pacheco[71], D. Pakk Selmi-Dei[16], M. Palatka[25], J. Pallotta[2], N. Palmieri[37], G. Parente[73], E. Parizot[29], A. Parra[73], S. Pastor[69], T. Paul[86], M. Pech[25], J. Pękala[61], R. Pelayo[53, 73], I.M. Pepe[19], L. Perrone[49], R. Pesce[42], E. Petermann[92], S. Petrera[43], A. Petrolini[42], Y. Petrov[79], C. Pfendner[94], R. Piegaia[3], T. Pierog[35], P. Pieroni[3], M. Pimenta[63], V. Pirronello[47], M. Platino[7], M. Plum[39], V.H. Ponce[1], M. Pontz[41], A. Porcelli[35], P. Privitera[90], M. Prouza[25], E.J. Quel[2], S. Querchfeld[34], J. Rautenberg[34], O. Ravel[33], D. Ravignani[7], B. Revenu[33], J. Ridky[25], S. Riggi[73], M. Risse[41], P. Ristori[2], H. Rivera[44], V. Rizi[43], J. Roberts[85], W. Rodrigues de Carvalho[73], G. Rodriguez[73], I. Rodriguez Cabo[73], J. Rodriguez Martino[9], J. Rodriguez Rojo[9], M.D. Rodríguez-Frías[71], G. Ros[71], J. Rosado[70], T. Rossler[26],

M. Roth[35], B. Rouillé-d'Orfeuil[90], E. Roulet[1], A.C. Rovero[5], C. Rühle[36], A. Saftoiu[64], F. Salamida[28], H. Salazar[53], F. Salesa Greus[79], G. Salina[46], F. Sánchez[7], C.E. Santo[63], E. Santos[63], E.M. Santos[21], F. Sarazin[78], B. Sarkar[34], S. Sarkar[74], R. Sato[9], N. Scharf[39], V. Scherini[44], H. Schieler[35], P. Schiffer[40, 39], A. Schmidt[36], O. Scholten[58], H. Schoorlemmer[57, 59], J. Schovancova[25], P. Schovánek[25], F. Schröder[35], D. Schuster[78], S.J. Sciutto[4], M. Scuderi[47], A. Segreto[50], M. Settimo[41], A. Shadkam[83], R.C. Shellard[13], I. Sidelnik[7], G. Sigl[40], H.H. Silva Lopez[56], O. Sima[65], A. 'Smiałkowski[62], R. Šmída[35], G.R. Snow[92], P. Sommers[88], J. Sorokin[12], H. Spinka[76, 81], R. Squartini[9], Y.N. Srivastava[86], S. Stanic[68], J. Stapleton[87], J. Stasielak[61], M. Stephan[39], A. Stutz[32], F. Suarez[7], T. Suomijärvi[28], A.D. Supanitsky[5], T. Šuša[23], M.S. Sutherland[83], J. Swain[86], Z. Szadkowski[62], M. Szuba[35], A. Tapia[7], M. Tartare[32], O. Taşcău[34], R. Tcaciuc[41], N.T. Thao[96], D. Thomas[79], J. Tiffenberg[3], C. Timmermans[59, 57], W. Tkaczyk[62 ‡], C.J. Todero Peixoto[14], G. Toma[64], L. Tomankova[25], B. Tomé[63], A. Tonachini[48], G. Torralba Elipe[73], P. Travnicek[25], D.B. Tridapalli[15], G. Tristram[29], E. Trovato[47], M. Tueros[73], R. Ulrich[35], M. Unger[35], M. Urban[30], J.F. Valdés Galicia[56], I. Valiño[73], L. Valore[45], G. van Aar[57], A.M. van den Berg[58], S. van Velzen[57], A. van Vliet[40], E. Varela[53], B. Vargas Cárdenas[56], J.R. Vázquez[70], R.A. Vázquez[73], D. Veberič[68, 67], V. Verzi[46], J. Vicha[25], M. Videla[8], L. Villaseñor[55], H. Wahlberg[4], P. Wahrlich[12], O. Wainberg[7, 11], D. Walz[39], A.A. Watson[75], M. Weber[36], K. Weidenhaupt[39], A. Weindl[35], F. Werner[35], S. Westerhoff[94], B.J. Whelan[88, 12], A. Widom[86], G. Wieczorek[62], L. Wiencke[78], B. Wilczyńska[61], H. Wilczyński[61], M. Will[35], C. Williams[90], T. Winchen[39], M. Wommer[35], B. Wundheiler[7], T. Yamamoto[90 a], T. Yapici[84], P. Younk[41, 82], G. Yuan[83], A. Yushkov[73], B. Zamorano Garcia[72], E. Zas[73], D. Zavrtanik[68, 67], M. Zavrtanik[67, 68], I. Zaw[85 h], A. Zepeda[54 b], J. Zhou[90], Y. Zhu[36], M. Zimbres Silva[34, 16], M. Ziolkowski[41]

[1] Centro Atómico Bariloche and Instituto Balseiro (CNEA-UNCuyo-CONICET), San Carlos de Bariloche, Argentina

[2] Centro de Investigaciones en Láseres y Aplicaciones, CITEDEF and CONICET, Argentina

[3] Departamento de Física, FCEyN, Universidad de Buenos Aires y CONICET, Argentina

[4] IFLP, Universidad Nacional de La Plata and CONICET, La Plata, Argentina

[5] Instituto de Astronomía y Física del Espacio (CONICET-UBA), Buenos Aires, Argentina

[6] Instituto de Física de Rosario (IFIR) - CONICET/U.N.R. and Facultad de Ciencias Bioquímicas y Farmacéuticas U.N.R., Rosario, Argentina

[7] Instituto de Tecnologías en Detección y Astropartículas (CNEA, CONICET, UNSAM), Buenos Aires,

Argentina

[8] National Technological University, Faculty Mendoza (CONICET/CNEA), Mendoza, Argentina

[9] Observatorio Pierre Auger, Malargüe, Argentina

[10] Observatorio Pierre Auger and Comisión Nacional de Energía Atómica, Malargüe, Argentina

[11] Universidad Tecnológica Nacional - Facultad Regional Buenos Aires, Buenos Aires, Argentina

[12] University of Adelaide, Adelaide, S.A., Australia

[13] Centro Brasileiro de Pesquisas Fisicas, Rio de Janeiro, RJ, Brazil

[14] Universidade de São Paulo, Instituto de Física, São Carlos, SP, Brazil

[15] Universidade de São Paulo, Instituto de Física, São Paulo, SP, Brazil

[16] Universidade Estadual de Campinas, IFGW, Campinas, SP, Brazil

[17] Universidade Estadual de Feira de Santana, Brazil

[18] Universidade Estadual do Sudoeste da Bahia, Vitoria da Conquista, BA, Brazil

[19] Universidade Federal da Bahia, Salvador, BA, Brazil

[20] Universidade Federal do ABC, Santo André, SP, Brazil

[21] Universidade Federal do Rio de Janeiro, Instituto de Física, Rio de Janeiro, RJ, Brazil

[22] Universidade Federal Fluminense, EEIMVR, Volta Redonda, RJ, Brazil

[23] Rudjer Boškovi'c Institute, 10000 Zagreb, Croatia

[24] Charles University, Faculty of Mathematics and Physics, Institute of Particle and Nuclear Physics, Prague, Czech Republic

[25] Institute of Physics of the Academy of Sciences of the Czech Republic, Prague, Czech Republic

[26] Palacky University, RCPTM, Olomouc, Czech Republic

[28] Institut de Physique Nucléaire d'Orsay (IPNO), Université Paris 11, CNRS-IN2P3, Orsay, France

[29] Laboratoire AstroParticule et Cosmologie (APC), Université Paris 7, CNRS-IN2P3, Paris, France

[30] Laboratoire de l'Accélérateur Linéaire (LAL), Université Paris 11, CNRS-IN2P3, France

[31] Laboratoire de Physique Nucléaire et de Hautes Energies (LPNHE), Universités Paris 6 et Paris 7, CNRS-IN2P3, Paris, France

[32] Laboratoire de Physique Subatomique et de Cosmologie (LPSC), Université Joseph Fourier Grenoble, CNRS-IN2P3, Grenoble INP, France

[33] SUBATECH, École des Mines de Nantes, CNRS-IN2P3, Université de Nantes, France

[34] Bergische Universität Wuppertal, Wuppertal, Germany

[35] Karlsruhe Institute of Technology - Campus North - Institut für Kernphysik, Karlsruhe, Germany

[36] Karlsruhe Institute of Technology - Campus North - Institut für Prozessdatenverarbeitung und Elektronik, Karlsruhe, Germany

[37] Karlsruhe Institute of Technology - Campus South - Institut für Experimentelle Kernphysik (IEKP), Karlsruhe, Germany

[38] Max-Planck-Institut für Radioastronomie, Bonn, Germany

[39] RWTH Aachen University, III. Physikalisches Institut A, Aachen, Germany

[40] Universität Hamburg, Hamburg, Germany

[41] Universität Siegen, Siegen, Germany

[42] Dipartimento di Fisica dell'Università and INFN, Genova, Italy

[43] Università dell'Aquila and INFN, L'Aquila, Italy

[44] Università di Milano and Sezione INFN, Milan, Italy

[45] Università di Napoli "Federico II" and Sezione INFN, Napoli, Italy

[46] Università di Roma II "Tor Vergata" and Sezione INFN, Roma, Italy

[47] Università di Catania and Sezione INFN, Catania, Italy

[48] Università di Torino and Sezione INFN, Torino, Italy

[49] Dipartimento di Matematica e Fisica "E. De Giorgi" dell'Università del Salento and Sezione INFN, Lecce, Italy

[50] Istituto di Astrofisica Spaziale e Fisica Cosmica di Palermo (INAF), Palermo, Italy

[51] Istituto di Fisica dello Spazio Interplanetario (INAF), Università di Torino and Sezione INFN, Torino, Italy

[52] INFN, Laboratori Nazionali del Gran Sasso, Assergi (L'Aquila), Italy

[53] Benemérita Universidad Autónoma de Puebla, Puebla, Mexico

[54] Centro de Investigación y de Estudios Avanzados del IPN (CINVESTAV), México, Mexico

[55] Universidad Michoacana de San Nicolas de Hidalgo, Morelia, Michoacan, Mexico

[56] Universidad Nacional Autonoma de Mexico, Mexico, D.F., Mexico

[57] IMAPP, Radboud University Nijmegen, Netherlands

[58] Kernfysisch Versneller Instituut, University of Groningen, Groningen, Netherlands

[59] Nikhef, Science Park, Amsterdam, Netherlands

[60] ASTRON, Dwingeloo, Netherlands

[61] Institute of Nuclear Physics PAN, Krakow, Poland

[62] University of Łódź, Łódź, Poland

[63] LIP and Instituto Superior Técnico, Technical University of Lisbon, Portugal

[64] 'Horia Hulubei' National Institute for Physics and Nuclear Engineering, Bucharest- Magurele, Romania

[65] University of Bucharest, Physics Department, Romania

[66] University Politehnica of Bucharest, Romania

[67] J. Stefan Institute, Ljubljana, Slovenia

[68] Laboratory for Astroparticle Physics, University of Nova Gorica, Slovenia

[69] Instituto de Física Corpuscular, CSIC-Universitat de València, Valencia, Spain

[70] Universidad Complutense de Madrid, Madrid, Spain

[71] Universidad de Alcalá, Alcalá de Henares (Madrid), Spain

[72] Universidad de Granada & C.A.F.P.E., Granada, Spain

[73] Universidad de Santiago de Compostela, Spain

[74] Rudolf Peierls Centre for Theoretical Physics, University of Oxford, Oxford, United Kingdom

[75] School of Physics and Astronomy, University of Leeds, United Kingdom

[76] Argonne National Laboratory, Argonne, IL, USA

[77] Case Western Reserve University, Cleveland, OH, USA

[78] Colorado School of Mines, Golden, CO, USA

[79] Colorado State University, Fort Collins, CO, USA

[80] Colorado State University, Pueblo, CO, USA

[81] Fermilab, Batavia, IL, USA

[82] Los Alamos National Laboratory, Los Alamos, NM, USA

[83] Louisiana State University, Baton Rouge, LA, USA

[84] Michigan Technological University, Houghton, MI, USA

[85] New York University, New York, NY, USA

[86] Northeastern University, Boston, MA, USA

[87] Ohio State University, Columbus, OH, USA

[88] Pennsylvania State University, University Park, PA, USA

[90] University of Chicago, Enrico Fermi Institute, Chicago, IL, USA

[91] University of Hawaii, Honolulu, HI, USA

[92] University of Nebraska, Lincoln, NE, USA

[93] University of New Mexico, Albuquerque, NM, USA

[94] University of Wisconsin, Madison, WI, USA

[95] University of Wisconsin, Milwaukee, WI, USA

[96] Institute for Nuclear Science and Technology (INST), Hanoi, Vietnam

(‡) Deceased

(a) at Konan University, Kobe, Japan

(b) now at the Universidad Autonoma de Chiapas on leave of absence from Cinvestav

(f) now at University of Maryland

(h) now at NYU Abu Dhabi

(i) now at Université de Lausanne

1. Introduction

Establishing at which energy the intensity of extragalactic cosmic rays starts to dominate the intensity of galactic ones would constitute an important step forward to provide further understanding on the origin of Ultra-High Energy Cosmic Rays (UHECRs). A time honored picture is that the *ankle*, a hardening of the energy spectrum located at $\simeq$ 4 EeV (Linsley 1963; Lawrence *et al.* 1991; Nagano *et al.* 1992; Bird *et al.* 1993; Pierre Auger Collaboration 2010a) (where 1 EeV $\equiv 10^{18}$ eV), is the onset in the energy spectrum marking the transition between galactic and extragalactic UHECRs (Linsley 1963). As a natural signature of the escape of cosmic rays from the Galaxy, large scale anisotropies in the distribution of arrival directions could be detected at energies below this spectral feature. Both the amplitude and the shape of such patterns are uncertain, as they depend on the model adopted to describe the regular and turbulent components of the galactic magnetic field, the charges of the cosmic rays, and the assumed distribution of sources in space and time. For cosmic rays mostly heavy and originating from stationary sources located in the galactic disk, some estimates based on diffusion and drift motions (Ptuskin *et al.* 1993; Candia *et al.* 2003) as well as direct integration of trajectories (Zirakashvili *et al.* 1998; Giacinti *et al.* 2011) show that dipolar anisotropies at the level of a few percents could be imprinted in the energy range just below the ankle energy. Even larger amplitudes could be left in case of light primaries, unless sources are strongly intermittent and pure diffusion motions hold up to EeV energies (Calvez *et al.* 2010; Eichler & Pohl 2011).

If UHECRs above 1 EeV have already a predominant extragalactic origin (Hillas 1967; Blumenthal 1970; Berezinsky *et al.* 2006; Berezinsky *et al.* 2004), their angular distribution is expected to be isotropic to a high level. But, even for isotropic extragalactic cosmic rays, the translational motion of the Galaxy relative to a possibly stationary extragalactic cosmic ray rest frame can produce a dipole in a similar way to the *Compton-Getting effect* (Compton & Getting 1935) which has been measured with cosmic rays of much lower energy at the solar time scale (Cutler & Groom 1986; Amenomori *et al.* 2006; Abdo *et al.* 2009; Aglietta *et al.* 2009; Abbasi *et al.* 2010) as a result of the Earth moving relative to the frame in which the cosmic rays have no bulk motion. Moreover, the rotation of the Galaxy can also produce anisotropy by virtue of moving magnetic fields, as cosmic rays travelling through far away regions of the Galaxy experience an electric force due to the relative motion of the system in which the field is purely magnetic (Harari *et al.* 2010). The large scale structure of the galactic magnetic field is expected to transform even a simple Compton-Getting dipole into a more complex anisotropy at Earth, described by higher order multipoles (Harari *et al.* 2010). A quantitative estimate of the imprinted pattern would require knowledge of the global structure of the galactic magnetic field and the charges of the particles, as well as the frame in which extragalactic cosmic rays have no bulk motion. If, for instance, the frame in which the UHECR distribution is isotropic coincides with the cosmic microwave background rest frame, the amplitude of the simple Compton-Getting dipole would be about 0.6% (Kachelriess & Serpico 2006). The same order of magnitude is expected if UHECRs have no bulk motion with respect to the local group of galaxies.

Scrutiny of the large scale distribution of arrival directions of UHECRs as a function of the energy is thus one important observable to provide key elements for understanding their origin in the EeV energy range. Using the large amount of data collected by the Surface Detector (SD) array of the Pierre Auger Observatory, results of first harmonic analysis of the right ascension distribution performed in different energy ranges above 0.25 EeV were recently reported (Pierre Auger Collaboration 2011a). Upper limits on the dipole component in the equatorial plane were derived, being below 2% at 99% *C.L.* for EeV energies and providing the most stringent bounds ever obtained. These analyses benefit from the almost uniform directional exposure in right ascension of the SD array of the Pierre Auger Observatory which is due to the Earth rotation, and they constitute a powerful tool for picking up any dipolar modulation in this coordinate. However, since this technique is not sensitive to an eventual dipolar component along the Earth rotation axis, we aim in the present report at estimating not only the dipole component in the right ascension distribution but also the component along the Earth rotation axis as well. More generally, we present a comprehensive search in all direction for any dipole or quadrupole patterns significantly standing out above the background noise.

Searching for anisotropies with relative amplitudes down to the percent level requires the control of the exposure of the experiment at even greater accuracy. Spurious modulations in the right ascension distribution are induced by the variations of the effective size of the SD array with time and by the variations of the counting rate of events due to the changes of atmospheric conditions. In Ref. (Pierre Auger Collaboration 2011a), we showed in a quantitative way that such effects can be properly accounted for by making use of the instantaneous status of the SD array provided each second by the monitoring system, and by converting the observed signals in actual atmospheric conditions into the ones that would have been measured at some given reference atmospheric conditions. Searching for anisotropies explicitly in declination requires the control of additional systematic errors affecting both the directional exposure of the Observatory and the counting rate of events in local angles. Each of these additional effects are carefully presented in sections 3 and 4.

After correcting for the experimental effects, searches for large scale patterns above 1 EeV are presented in section 5. Additional cross-checks against eventual systematic errors affecting the results obtained in section 5 are presented in section 6. Resulting upper limits on dipole and quadrupole amplitudes are presented and discussed in section 7, while a final summary is given in section 8. Some further technical aspects are detailed in the appendices.

2. The Pierre Auger Observatory and the data set

The Pierre Auger Observatory (Pierre Auger Collaboration 2004) is located in Malargüe, Argentina, at mean latitude 35.2° S, mean longitude 69.5° W and mean altitude 1400 meters above sea level. Two complementary techniques are used to detect extensive air showers initiated by UHECRs : a *surface detector array* and a *fluorescence detector*. The SD array consists of 1660 water-Cherenkov detectors covering an area of about 3000 km^2 on a triangular grid with 1.5 km spacing, allowing electrons, photons and muons in air showers to be sampled at ground level with a duty cycle of almost 100%. In addition, the atmosphere above the SD array is observed during dark cloudless nights by 27 optical telescopes grouped in 5 buildings. These detectors observe the longitudinal profile of air showers by detecting the fluorescence light emitted by nitrogen molecules excited by the cascade.

The data set analysed here consists of events recorded by the SD array from 1 January 2004 to 31 December 2011. During this time, the size of the Observatory increased from 154 to 1660 water-Cherenkov detectors. Events used in this analysis have zenith angles less than 55°. Moreover, an event is accepted only if all six nearest neighbours of the water-Cherenkov detector with the highest signal were operational at the time of the event. This fiducial cut ensures good event reconstruction (Pierre Auger Collaboration 2010b). Throughout this article, based on this fiducial cut, any active water-Cherenkov detector with six active neighbours will be defined as an *elemental cell.* Also, periods of array instability have been omitted from the data set, reducing the duty cycle to $\simeq 90\%$. Above the energy at which the detection efficiency saturates, 3 EeV (Pierre Auger Collaboration 2010b), and restricting the zenith angle between 0 and 55°, the total exposure of the SD array is 23,555 km^2 yr sr for the eight years considered in this analysis.

The event direction is determined from a fit to the arrival times of the shower front at the SD, which requires having at least three triggered stations. The precision achieved in this reconstruction depends upon the GPS clock resolution and on the fluctuations in the time of arrival of the first particle (Bonifazi *et al.* 2008). The angular resolution of events having only three triggered detectors (*i.e.* those at the lowest energies observed) is about 2.2°, which is largely sufficient to perform searches for large-scale patterns in arrival directions, and reaches $\sim 1°$ for events with multiplicities larger than five (Bonifazi *et al.* 2009). The energy of each event is determined in a two-step procedure. First, using the constant intensity cut method, the shower size at a reference distance of 1000 m, $S(1000)$, is converted to the value S_{38° that would have been expected had the shower arrived at a zenith angle 38°. Then, S_{38° is converted to energy using a calibration curve based on hybrid events measured simultaneously by the SD array and the fluorescence telescopes which can provide a calorimetric measurement of the energy (Pierre Auger Collaboration 2008). The uncertainty in S_{38° resulting from the fit of the shower size, the conversion to a reference angle, the fluctuations from shower-to-shower and the calibration curve amounts to about 15%. The absolute energy scale is given by the fluorescence measurements and has a systematic uncertainty of 22% (Pierre Auger Collaboration 2008).

3. Control of the event counting rate

The control of the event counting rate is critical in searches for large scale anisotropies. Due to the steepness of the energy spectrum, any mild bias in the estimate of the shower energy with time or incident angles can lead to significant distortions of the event counting rate. The procedure followed to obtain an unbiased estimate of the shower energy is described in this section. This procedure consists in correcting measurements of shower sizes, $S(1000)$, for the influence of weather effects and of the geomagnetic field *before* the conversion to S_{38° using the constant intensity method. Then, the conversion to energy is applied.

3.1. Influence of atmospheric conditions on shower size

Changes in the atmospheric pressure, P, and air density, ρ, have been shown to affect the development of extensive air showers detected by the surface detector array and these changes are reflected in the temporal variations of shower size at a fixed energy (Pierre Auger Collaboration 2009). To eliminate these variations, the procedure used to convert the observed signal into energy needs to account for these atmospheric effects. This is performed by relating the shower size $S(1000)$, measured at the actual density ρ and pressure P, to the one $S_{atm}(1000)$ that would have been measured at reference values ρ_0 and P_0, chosen as the average values at Malargüe (*i.e.* $\rho_0 = 1.06$ kg m^{-3} and $P_0 = 862$ hPa (Pierre Auger Collaboration 2009)) :

$$S_{atm}(1000) = [1 - \alpha_P(\theta)(P - P_0) - \alpha_\rho(\theta)(\rho_d - \rho_0) - \beta_\rho(\theta)(\rho - \rho_d)]\, S(1000), \tag{1}$$

where ρ_d is the average daily density at the time the event was recorded. The measured coefficients α_ρ, β_ρ and α_P - given in Table 1 - reflect respectively the impact of the variation of air density (and thus temperature) at long and short time scales, and of the variation of pressure on the shower sizes. Coefficients related to the air density are here predominant relative to the ones related to the pressure.

$\sec\theta$	α_ρ[kg^{-1}m^3]	β_ρ[kg^{-1}m^3]	α_P[hPa^{-1}]
[1.0 – 1.2]	$-9.7\ 10^{-1}$	$-2.6\ 10^{-1}$	$-4.4\ 10^{-4}$
[1.2 – 1.4]	$-7.2\ 10^{-1}$	$-2.2\ 10^{-1}$	$-1.6\ 10^{-3}$
[1.4 – 1.6]	$-5.4\ 10^{-1}$	$-2.0\ 10^{-1}$	$-2.3\ 10^{-3}$
[1.6 – 1.8]	$-4.0\ 10^{-1}$	$-4.3\ 10^{-2}$	$-1.9\ 10^{-3}$
[1.8 – 2.0]	$-1.5\ 10^{-1}$	$-2.3\ 10^{-2}$	$-2.8\ 10^{-3}$

Table 1: Coefficients α_ρ, β_ρ and α_P used to correct shower sizes for atmospheric effects on shower development, in bins of $\sec\theta$. From Ref (Pierre Auger Collaboration 2009).

Applying these corrections to the energy assignments of showers allows us to cancel spurious variations of the event rate in right ascension, whose typical amplitudes amount to a few per thousand when considering data sets collected over full years.

3.2. Influence of the geomagnetic field on shower size

The trajectories of charged particles in extensive air showers are curved in the Earth's magnetic field, resulting in a broadening of the spatial distribution of particles in the direction of the Lorentz force. As the strength of the geomagnetic field component perpendicular to any arrival direction depends on both the zenith and azimuthal angles, the small changes of the density of particles at ground induced by the field break the circular symmetry of the lateral spread of the particles and thus induce a dependence of the shower size $S(1000)$ at a fixed energy in terms of the azimuthal angle. Due to the steepness of the energy spectrum, such an azimuthal dependence translates into azimuthal modulations of the estimated cosmic ray event rate at a given $S(1000)$. To eliminate these effects, the observed shower size $S(1000)$ is related to the one that would have been observed in the absence of geomagnetic field $S_{geom}(1000)$ (Pierre Auger Collaboration 2011b) :

$$S_{geom}(1000) = \left[1 - g_1 \cos^{-g_2}(\theta) \sin^2(\widehat{\mathbf{u},\mathbf{b}})\right] S(1000), \tag{2}$$

where $g_1 = (4.2 \pm 1)\ 10^{-3}$, $g_2 = 2.8 \pm 0.3$, and $\mathbf{u}$ and $\mathbf{b} = \mathbf{B}/\|\mathbf{B}\|$ denote the unit vectors in the shower direction and the geomagnetic field direction, respectively. At a zenith angle $\theta = 55°$, the amplitude of the asymmetry in azimuth already amounts to $\simeq 2\%$, which is why we restrict the present analysis to zenith angles smaller than this value. Carrying out these corrections is thus critical for performing large scale anisotropies measurements in declination.

3.3. From shower size to energy

Once the influence on $S(1000)$ of weather and geomagnetic effects are accounted for, the dependence of $S(1000)$ on zenith angle due to the attenuation of the shower and geometrical effects is extracted from the data using the constant intensity cut method (Pierre Auger Collaboration 2008). The attenuation curve $CIC(\theta)$ is fitted with a second order polynomial in $x = \cos^2(\theta) - \cos^2(38°)$: $CIC(\theta) = 1 + ax + bx^2$. The angle 38° is chosen as a reference to convert $S(1000)$ to $S_{38°} = S(1000)/CIC(\theta)$. $S_{38°}$ may be regarded as the signal that would have been expected had the shower arrived at 38°. The values of the parameters

$a = 0.94 \pm 0.03$ and $b = -0.95 \pm 0.05$ are deduced for $S_{38^\circ} = 22$ VEM[1], that corresponds to an energy of about 4 EeV - just above the threshold energy for full efficiency. The differences of these parameters with respect to previous reports will be discussed in section 6.

Finally, the sub-sample of events recorded by both the fluorescence telescopes and the SD array is used to establish the relationship between the energy reconstructed with the fluorescence telescopes E_{FD} and S_{38° : $E_{FD} = AS_{38^\circ}^{B}$. The resulting parameters from the data fit are $A = (1.68 \pm 0.05) \times 10^{-1}$ EeV and $B = 1.030 \pm 0.009$, in good agreement with the recent report given in Ref. (Pesce *et al.* 2011). The energy scale inferred from this data sample is applied to all showers detected by the SD array.

4. Directional exposure of the Surface Detector array above 1 EeV

The *directional exposure* ω of the Observatory provides the effective time-integrated collecting area for a flux from each direction of the sky [2], in units km^2 yr. For energies below 3 EeV, it is controlled by the detection efficiency ϵ for triggering. This efficiency depends on the energy E, the zenith angle θ, and the azimuth angle φ. Consequently, the directional exposure of the Observatory is maximal above 3 EeV, and it is less at lower energies where the detection efficiency is less than unity.

In this section, we show in a comprehensive way how the directional exposure of the SD array is obtained as a function of the energy. First, we explain how the slightly non-uniform exposure of the sky in sidereal time can be accounted for in the search for anisotropies (section 4.1). In section 4.2, we empirically calculate the detection efficiency as a function of the zenith angle and deduce the exposure below the full efficiency energy (3 EeV). In section 4.3, we discuss the azimuthal dependence of the efficiency due to the geomagnetic effects, introduce the corrections due to the tilt of the array in section 4.4 and the corrections due to the spatial extension of the array in section 4.5, and show that the influence of weather effects is negligible on the detection efficiency between 1 and 3 EeV in section 4.6. Finally we give in section 4.7 some examples of our fully corrected exposure at several energies.

---

[1] A vertical equivalent muon, or VEM, is the expected signal in a surface detector crossed by a muon traveling vertically and centrally to it

[2] In other contexts such as the determination of the energy spectrum for instance, the term ”exposure” refers to the *total* exposure integrated over the celestial sphere, in units km^2 yr sr.

4.1. From local to celestial directional exposure.

The choice of the fiducial cut to select high quality events allows the precise determination of the geometric directional aperture per cell as $a_{\rm cell}(\theta) = 1.95\ \cos\theta$ km^2 (Pierre Auger Collaboration 2010b). It also allows us to exploit the regularity of the array for obtaining its geometric directional aperture as a simple multiple of $a_{\rm cell}(\theta)$ (Pierre Auger Collaboration 2010b). The number of elemental cells $n_{\rm cell}(t)$ is recorded every second using the trigger system of the Observatory. It reflects the array growth as well as the dead periods of each detector. To search for celestial large scale anisotropies, it is mandatory to account for the modulation imprinted by the variations of $n_{\rm cell}(t)$ in the expected number of events at the *sidereal periodicity* T_{sid}. Within each sidereal day, we denote throughout this article by α^0 the local sidereal time and express it in hours or in radians, as appropriate. For practical reasons, α^0 is chosen so that it is always equal to the right ascension of the zenith at the centre of the array. As a function of α^0, the total number of elemental cells $N_{\rm cell}(\alpha^0)$ and its associated relative variations $\Delta N_{\rm cell}(\alpha^0)$ are then obtained from :

$$N_{\rm cell}(\alpha^0) = \sum_j n_{\rm cell}(\alpha^0 + jT_{sid}), \qquad \Delta N_{\rm cell}(\alpha^0) = \frac{N_{\rm cell}(\alpha^0)}{\langle N_{\rm cell}(\alpha^0)\rangle}, \tag{3}$$

with $\big\langle N_{\rm cell}(\alpha^0)\big\rangle = 1/T_{sid}\int_0^{T_{sid}} {\rm d}\alpha^0 N_{\rm cell}(\alpha^0)$. In the same way as in Ref. (Pierre Auger Collaboration 2011a), the small modulation of the expected number of events in right ascension induced by those variations will be accounted for by weighting each event k with a factor inversely proportional to $\Delta N_{\rm cell}(\alpha^0_k)$ when estimating the anisotropy parameters in section 5. Placing such time dependences in the event weights allows us to remove the modulations in time imprinted by the growth of the array and the dead times for each detector.

At any time, the *effective* directional aperture of the SD array is controlled by the geometric one *and* the detection efficiency function $\epsilon(\theta,\varphi,E)$. For each elemental cell, the directional exposure in celestial coordinates is then simply obtained through the integration over local sidereal time of $x^{(i)}(\alpha^0)\times a_{\rm cell}(\theta)\times\epsilon(\theta,\varphi,E)$, where $x^{(i)}(\alpha^0)$ is the operational time of the cell (i). Actually, since the small modulations in time imprinted in the event counting rate by experimental effects will be accounted for by means of the weighting procedure just described when searching for anisotropies, the small variations in local sidereal time for each $x^{(i)}(\alpha^0)$ can be neglected in calculating ω. The zenith and azimuth angles are related to the declination and the right ascension through :

$$\begin{aligned} \cos\theta &= \sin\delta\sin\ell_{\rm site} + \cos\delta\cos\ell_{\rm site}\cos{(\alpha-\alpha^0)}, \\ \tan\varphi &= \frac{\cos\delta\sin\ell_{\rm site}\cos{(\alpha-\alpha^0)} - \sin\delta\cos\ell_{\rm site}}{\cos\delta\sin{(\alpha-\alpha^0)}}, \end{aligned} \tag{4}$$

with $\ell_{\rm site}$ the mean latitude of the Observatory. Since both θ and φ depend only on the difference $\alpha-\alpha^0$, the integration over α^0 can then be substituted for an integration over the hour angle $\alpha' = \alpha - \alpha^0$ so that actually, the directional exposure does not depend on right ascension when the $x^{(i)}$ are assumed local sidereal time independent :

$$\omega(\delta, E) = \sum_{i=1}^{n_{\mathrm{cell}}} x^{(i)} \int_0^{24h} \mathrm{d}\alpha' \, a_{\mathrm{cell}}(\theta(\alpha', \delta)) \; \epsilon(\theta(\alpha', \delta), \varphi(\alpha', \delta), E). \tag{5}$$

Above 3 EeV, this integration can be performed analytically (Sommers 2001). Below 3 EeV, the non-saturation of the detection efficiency makes the directional exposure lower. Next sub-sections are dedicated to the determination of $\epsilon(\theta, \varphi, E)$.

4.2. Detection efficiency

To determine the detection efficiency function, a natural method would be to generate showers by means of Monte-Carlo simulations and to calculate the ratio of the number of triggered events to the total simulated. However, there are discrepancies in the predictions of the hadronic interaction model regarding the number of muons in shower simulations and what is found in our data (Engel *et al.* 2007). This prevents us from relying on this method for obtaining the detection efficiency to the required accuracy.

We adopt here instead an empirical approach, based on the quasi-invariance of the zenithal distribution to large scale anisotropies for zenith angles less than $\simeq 60°$ and for any Observatory whose latitude is far from the poles of the Earth. For full efficiency, the distribution in zenith angles $\mathrm{d}N/\mathrm{d}\theta$ is proportional to $\sin\theta\cos\theta$ for solid angle and geometry reasons, so that the distribution in $\mathrm{d}N/\mathrm{d}\sin^2\theta$ is uniform. Consequently, below full efficiency, *any significant deviation from a uniform behaviour in the* $\mathrm{d}N/\mathrm{d}\sin^2\theta$ *distribution provides an empirical measurement of the zenithal dependence of the detection efficiency.* The quasi-invariance of $\mathrm{d}N/\mathrm{d}\sin^2\theta$ to large scale anisotropies is demonstrated in Appendix A.

Based on this quasi-invariance, the detection efficiency averaged over the azimuth can be estimated from :

$$\langle \epsilon(\theta, \varphi, E) \rangle_\varphi = \frac{1}{\mathcal{N}} \frac{\mathrm{d}N(\sin^2\theta, E)}{\mathrm{d}\sin^2\theta}, \tag{6}$$

where the notation $\langle \cdot \rangle_\varphi$ stands for the average over φ and the constant $\mathcal{N}$ is the number of events that would have been observed at energy E and for any $\sin^2\theta$ value in case of full efficiency for an energy spectrum $\mathrm{d}N/\mathrm{d}E = 40 \ (E/\mathrm{EeV})^{-3.27} \ \mathrm{km}^{-2}\mathrm{yr}^{-1}\mathrm{sr}^{-1}\mathrm{EeV}^{-1}$ - as measured between 1 and 4 EeV (Pierre Auger Collaboration 2010a). Consequently, for each zenith angle, this empirical measurement

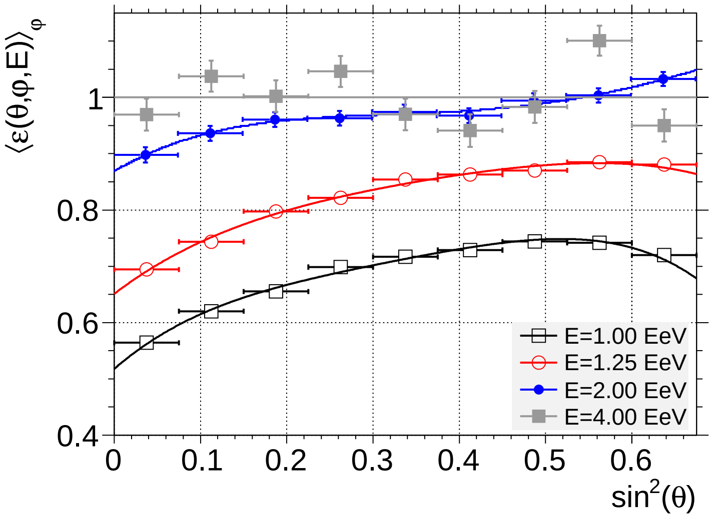

Fig. 1.— Detection efficiency averaged over the azimuth as a function of $\sin^2\theta$ at different energies, empirically measured from the data.

of the efficiency provides an estimate *relative* to the overall spectrum of cosmic rays. In particular, since it is applied to *all* events detected at energy E without distinction based on the primary mass of cosmic rays, this technique is not sensitive to evaluate the mass dependence of the detection efficiency. For that reason, the anisotropy searches reported in section 5 pertain to the whole population of cosmic rays, whether this population consists of a single primary mass or a mixture of several elements.

Results are shown in Fig. 1 for four different energies[3]. At 4 EeV, a uniform behaviour around 1 is observed, though quite noisy due to the reduced statistics. This uniform behaviour is consistent with full efficiency at this energy, as expected. At 2 EeV, a loss of efficiency is observed at small zenith angles while the muonic component of showers still ensures a recovering of efficiency above $\simeq 40°$. At lower energies, a loss of efficiency is observed at all zenith angles. In the following, we use parameterisations obtained by fitting each distribution with a fourth-order polynomial function in $\sin^2\theta$, which is sufficient to reproduce the main details as illustrated in Fig. 1.

---

[3] To get the detection efficiency at a single energy E, events are actually selected in narrow energy bins around E. In addition, to account for the energy spectrum in $E^{-3.27}$ in this energy range, each event is weighted by a factor $E^{3.27}$.

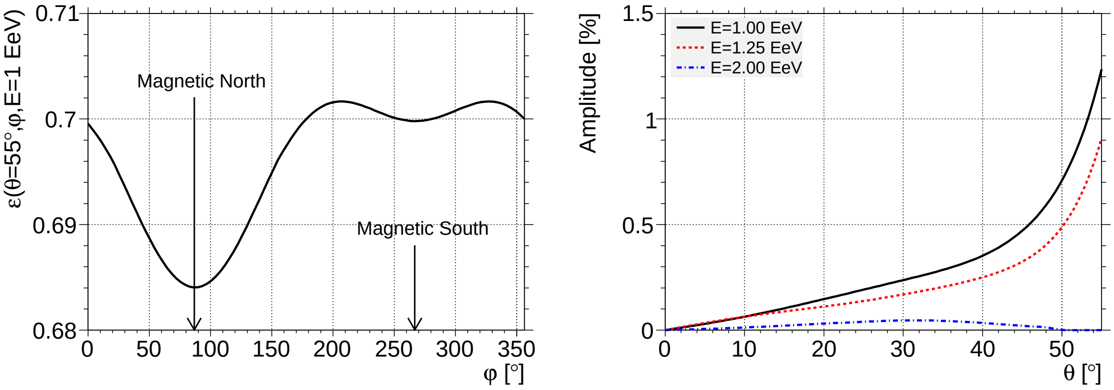

Fig. 2.— Left : Dependence of the detection efficiency on azimuth for $\theta = 55°$ and $E = 1$ EeV, due to geomagnetic effects. Right : Maximal contrast of the azimuthal modulation of the detection efficiency induced by geomagnetic effects as a function of the zenith angle.

4.3. Geomagnetic effects below full efficiency

In addition to the effects on the energy determination presented in section 3.2, geomagnetic effects also affect the detection efficiency for showers with energies below 3 EeV. This is because under any incident angles (θ, φ), a shower with an energy E triggers the SD array with a probability associated with its size which is a function of azimuth because of the geomagnetic effects [4] : $E \times (1 + \Delta(\theta, \varphi))^B$. Above 1 EeV, this effect is in fact the main source of azimuthal dependence of the detection efficiency, so that to first order in $\Delta(\theta, \varphi)$, $\epsilon(\theta, \varphi, E)$ can be estimated as :

$$\begin{aligned}\epsilon(\theta,\varphi,E) &= \frac{1}{\mathcal{N}}\frac{\mathrm{d}N(\sin^2\theta, E(1+\Delta(\theta,\varphi))^B)}{\mathrm{d}\sin^2\theta} \\ &\simeq \langle\epsilon(\theta,\varphi,E)\rangle_\varphi + \frac{BE\Delta(\theta,\varphi)}{\mathcal{N}}\frac{\partial\langle\epsilon(\theta,\varphi,E)\rangle_\varphi}{\partial E}. \qquad (7)\end{aligned}$$

The correction to the detection efficiency induced by geomagnetic effects, and in particular the azimuthal dependence, is thus straightforward to implement from the knowledge of $\langle\epsilon(\theta,\varphi,E)\rangle_\varphi$. An example of such an azimuthal dependence is shown in the left panel of Fig. 2, for $E = 1$ EeV and $\theta = 55°$. The modulation reflects the one due to the energy determination : the detection efficiency is lowered in the directions

---

[4] Here, the shorthand notation $\Delta(\theta, \varphi)$ stands for $g_1 \cos^{-g_2}(\theta) \left[\sin^2(\widehat{\mathbf{u},\mathbf{b}}) - \left\langle \sin^2(\widehat{\mathbf{u},\mathbf{b}}) \right\rangle_\varphi\right]$. The energy $E \times (1 + \Delta(\theta, \varphi))^B$ is actually the one that would have been obtained without correcting for geomagnetic effects.

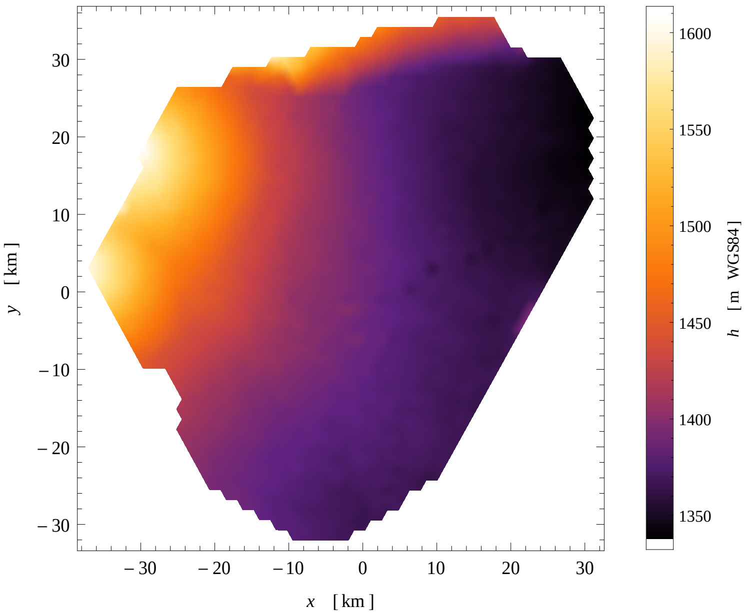

Fig. 3.— Colour-coded altitude (a.s.l.) of the water-Cherenkov detectors.

where the uncorrected energies are under-estimated due to geomagnetic effects, and the efficiency is higher where energies are over-estimated. The maximal contrast of such azimuthal modulations is displayed in the right panel as a function of the zenith angle, for three different energies. At 2 EeV, the amplitude slightly increases up to $\simeq 35°$, (below $\simeq 0.1\%$), and then decreases and even cancels due to the saturation of the detection efficiency. In contrast, when going down in energy, the relative amplitude largely increases with the zenith angle due to the increase of the derivative term, amounting to $\simeq 1.2\%$ for $\theta = 55°$ and $E = 1$ EeV.

4.4. Tilt of the array

The altitudes above sea level of the water-Cherenkov detectors are displayed in Fig. 3 in colour coding. The coordinates are in a Cartesian system whose origin is defined at the "centre" of the Observatory site. The Andes ridge building up in the western and north-western direction can be seen. A slightly tilted SD array gives rise to a small azimuthal asymmetry, and consequently slightly modifies the directional exposure with respect to Eqn. 5 through the little changes of the geometric directional aperture. This modification is twofold : the tilt changes the geometric factor $(\cos\theta)$ of the projected surface under incidence angles (θ, φ);

and also induces a compensating effect below full efficiency by slightly varying the detection efficiency with the azimuth angle φ.

Denoting $\mathbf{n}_\perp^{(\mathbf{i})}$ the normal vector to each elemental cell, the geometric directional aperture per cell is not any longer simply given by $\cos\theta$ but now depends on both θ and φ :

$$a_{\mathrm{cell}}^{(i)}(\theta,\varphi) = 1.95\ \mathbf{n}\cdot\mathbf{n}_\perp^{(\mathbf{i})} \simeq 1.95\ [1+\zeta^{(i)}\tan\theta\cos(\varphi-\varphi_0^{(i)})]\ \cos\theta, \tag{8}$$

where $\zeta^{(i)}$ and $\varphi_0^{(i)}$ are the zenith and azimuth angles of $\mathbf{n}_\perp^{(\mathbf{i})}$. It is actually this latter expression a_{cell} which has to be inserted into Eqn. 5 to calculate the directional exposure. Overall, the average tilt of the SD array is $\zeta^{\mathrm{eff}} \simeq 0.2°$, and induces a dipolar asymmetry in azimuth with a maximum in the downhill direction $\varphi_0^{\mathrm{eff}} \simeq 0°$ and with an amplitude increasing with the zenith angle as $\simeq 0.3\%\tan\theta$.

Below 3 EeV, the tilt of the array induces an additional variation of the detection efficiency with azimuth. This is because the effective separation between detectors for a given zenith angle depends now on the azimuth. Since, for a given zenith angle, the SD array seen by showers coming from the uphill direction is denser than that for those coming from the downhill direction, the detection efficiency is higher in the uphill direction. For an energy dependence of ϵ in $E^3/(E^3+E_{0.5}^3)$, we show in Appendix B that the change in the detection efficiency can be estimated as :

$$\Delta\epsilon_{\mathrm{tilt}}(\theta,\varphi,E) = \frac{E^3(E_{0.5}^3 - E_{0.5}^{\mathrm{tilt}^3}(\theta,\varphi))}{(E^3+E_{0.5}^3)(E^3+E_{0.5}^{\mathrm{tilt}^3}(\theta,\varphi))}, \tag{9}$$

where $E_{0.5}^{\mathrm{tilt}}(\theta,\varphi)$ is related to $E_{0.5}$ through :

$$E_{0.5}^{\mathrm{tilt}}(\theta,\varphi) \simeq E_{0.5}\times[1+\zeta^{\mathrm{eff}}\tan\theta\cos(\varphi-\varphi_0^{\mathrm{eff}})]^{3/2}. \tag{10}$$

Around 1 EeV, this correction tends to compensate the pure geometrical effect described above, and even overcompensates it at lower energies.

4.5. Spatial extension of the array

This spatial extension of the SD array is such that the range of latitudes covered by all cells reaches $\simeq 0.5°$. This induces a slightly different directional exposure between the cells located at the northern part of the array and the ones located at the southern part. This spatial extension can be accounted for to calculate the overall directional exposure using the cell latitudes $\ell_{\mathrm{cell}}^{(i)}$ instead of the mean site one in the transformations from local to celestial angles in Eqn. 4.

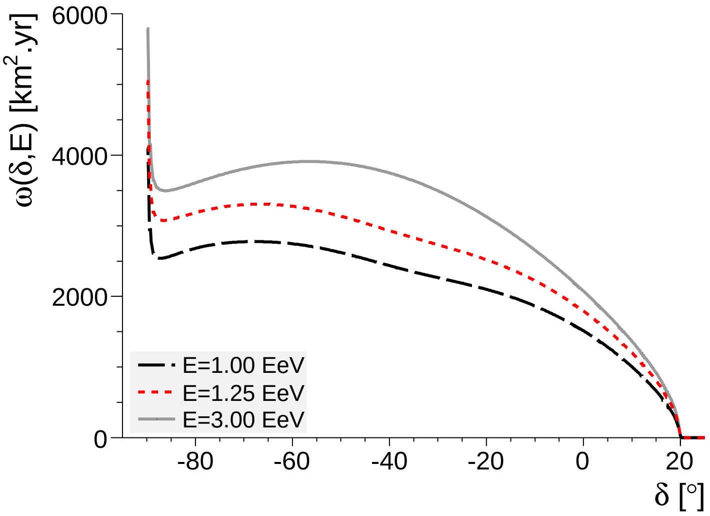

Fig. 4.— Directional exposure $\omega(\delta, E)$ as a function of the declination δ, for three different energies.

4.6. Weather effects below full efficiency

In the same way as geomagnetic effects, weather effects can also affect the detection efficiency for showers with energies below 3 EeV. However, *above* 1 EeV, we have shown in Ref. (Pierre Auger Collaboration 2011a) that as long as the analysis covers an integer number of years with almost equal exposure in every season, the amplitude of the spurious modulation in right ascension induced by this effect is small enough to be neglected when performing anisotropy analyses at the present level of sensitivity.

4.7. Final estimation of the directional exposure - Examples at some energies

Accounting for all effects, the final expression to calculate the directional exposure is slightly modified with respect to Eqn. 5 :

$$\omega(\delta, E) = \sum_{i=1}^{n_{\rm cell}} x^{(i)} \int_0^{24h} \mathrm{d}\alpha' \, a_{\rm cell}^{(i)}(\theta, \varphi) \;\; [\epsilon(\theta, \varphi, E) + \Delta\epsilon_{\rm tilt}(\theta, \varphi, E)]\,, \tag{11}$$

where both θ and φ depend on α', δ and $\ell_{\rm cell}^{(i)}$. The resulting dependence on declination is displayed in Fig. 4 for three different energies. Down to 1 EeV, the detection efficiency at high zenith angles is high enough that the equatorial south pole is visible at any time and hence constitutes the direction of maximum of exposure. For a wide range of declinations between $\simeq -89°$ and $\simeq -20°$, the directional exposure reaches

$\simeq 2,500$ km^2 yr at 1 EeV, and $\simeq 3,500$ km^2 yr for any energy above full efficiency. Then, at higher declinations, it smoothly falls to zero, so that no direction with declination above $\simeq 20°$ is visible.

The average expected number of events within any solid angle and any energy range can be recovered by integrating the directional exposure over the solid angle considered and the cosmic ray energy spectrum in the corresponding energy range. Note that the rapid variation of the exposure close to the South pole on an angular scale of the order of the angular resolution has no influence on the event counting rate, due to the quasi-zero solid angle in that particular direction. Consequently, though the exposure around the South pole could be affected by small changes of the detection efficiency around $\theta = 55°$, results presented in next sections are on the other hand *not* affected by the exact value of the exposure for declinations few degrees away from the South pole.

5. Searches for large scale patterns

5.1. Estimates of spherical harmonic coefficients

Any angular distribution over the sphere $\Phi(\mathbf{n})$ can be decomposed in terms of a multipolar expansion :

$$\Phi(\mathbf{n}) = \sum_{\ell \geq 0} \sum_{m=-\ell}^{\ell} a_{\ell m} Y_{\ell m}(\mathbf{n}), \tag{12}$$

where $\mathbf{n}$ denotes a unit vector taken in equatorial coordinates. The customary recipe to extract each multipolar coefficient makes use of the completeness relation of spherical harmonics :

$$a_{\ell m} = \int_{4\pi} \mathrm{d}\Omega \ \Phi(\mathbf{n}) Y_{\ell m}(\mathbf{n}), \tag{13}$$

where the integration is over the entire sphere of directions $\mathbf{n}$. Any anisotropy fingerprint is encoded in the $a_{\ell m}$ spherical harmonic coefficients. Variations on an angular scale of Θ radians contribute amplitude in the $\ell \leq 1/\Theta$ modes.

However, in case of partial sky coverage, the solid angle in the sky where the exposure is zero makes it impossible to estimate the multipolar coefficients $a_{\ell m}$ in this way. This is because the unseen solid angle prevents one from making use of the completeness relation of the spherical harmonics (Sommers 2001). Since the observed arrival direction distribution is in this case the *combination* of the angular distribution $\Phi(\mathbf{n})$ and of the directional exposure function $\omega(\mathbf{n})$, the integration performed in Eqn. 13 does not allow any longer the extraction of the multipolar coefficients of $\Phi(\mathbf{n})$, but only the ones of $\omega(\mathbf{n})\ \Phi(\mathbf{n})$ (Billoir & Deligny 2008) [5]:

$$\begin{aligned} b_{\ell m} &= \int_{\Delta\Omega} \mathrm{d}\Omega\ \omega(\mathbf{n})\Phi(\mathbf{n})Y_{\ell m}(\mathbf{n}) \\ &= \sum_{\ell'\geq 0}\sum_{m'=-\ell'}^{\ell'} a_{\ell' m'} \int_{\Delta\Omega} \mathrm{d}\Omega\ \omega(\mathbf{n})Y_{\ell' m'}(\mathbf{n})Y_{\ell m}(\mathbf{n}). \end{aligned} \tag{14}$$

Formally, the $a_{\ell m}$ coefficients appear related to the $b_{\ell m}$ ones through a convolution such that $b_{\ell m} = \sum_{\ell'\geq 0}\sum_{m'=-\ell'}^{\ell'} [K]_{\ell m}^{\ell' m'}\ a_{\ell' m'}$. The matrix K, which imprints the interferences between modes induced by the non-uniform and partial coverage of the sky, is entirely determined by the directional exposure. The relationship established in Eqn. 14 is valid for *any* exposure function $\omega(\mathbf{n})$.

Meanwhile, the observed arrival direction distribution, $\overline{\mathrm{d}N}(\mathbf{n})/\mathrm{d}\Omega$, provides a direct estimation of the $b_{\ell m}$ coefficients through (hereafter, we use an over-line to indicate the *estimator* of any quantity) :

$$\overline{b}_{\ell m} = \int_{\Delta\Omega} \mathrm{d}\Omega\ \frac{\overline{\mathrm{d}N}(\mathbf{n})}{\mathrm{d}\Omega}\ Y_{\ell m}(\mathbf{n}), \tag{15}$$

where the distribution $\overline{\mathrm{d}N}(\mathbf{n})/\mathrm{d}\Omega$ of any set of N arrival directions $\{\mathbf{n}_1, ..., \mathbf{n}_N\}$ can be modelled as a sum of Dirac functions on the sphere. Then, if the multipolar expansion of the angular distribution $\Phi(\mathbf{n})$ is *bounded* to $\ell_{\max}$, that is, if the $\Phi(\mathbf{n})$ has no higher moments than $\ell_{\max}$, the first $b_{\ell m}$ coefficients with $\ell \leq \ell_{\max}$ are related to the non-vanishing $a_{\ell m}$ by the square matrix $K_{\ell_{\max}}$ *truncated* to $\ell_{\max}$. Inverting this truncated matrix allows us to recover the underlying $a_{\ell m}$ from the measured $b_{\ell m}$ (with $\ell \leq \ell_{\max}$) :

$$\overline{a}_{\ell m} = \sum_{\ell'=0}^{\ell_{\max}}\sum_{m'=-\ell'}^{\ell'} [K_{\ell_{\max}}^{-1}]_{\ell m}^{\ell' m'} \overline{b}_{\ell' m'}. \tag{16}$$

In case of small anisotropies ($|a_{\ell m}|/a_{00} \ll 1$), the resolution on each recovered $\overline{a}_{\ell m}$ coefficient is proportional to $\left([K_{\ell_{\max}}^{-1}]_{\ell m}^{\ell m}\right)^{0.5}$ (Billoir & Deligny 2008) :

$$\sigma_{\ell m} = \left([K_{\ell_{\max}}^{-1}]_{\ell m}^{\ell m}\ \overline{a}_{00}\right)^{0.5}. \tag{17}$$

The dependence on $\ell_{\max}$ of the coefficients of $K_{\ell_{\max}}^{-1}$ induces an intrinsic indeterminacy of each recovered coefficient $\overline{a}_{\ell m}$ as $\ell_{\max}$ is increasing. This is nothing else but the mathematical translation of it being impossible to know the angular distribution of cosmic rays in the uncovered region of the sky.

---

[5] To cope with the unseen solid angle, another approach makes use of orthogonal functions of increasing multipolarity, tailored to the exposure ω itself (Billoir & Deligny 2008). This method would yield similar accuracies.

Henceforth, we adapt this general formalism to the search for anisotropies in Auger data in different energy intervals. We assume that the energy dependence of the angular distribution of cosmic rays is smooth enough that the multipolar coefficients can be considered constant for any energy E within a narrow interval ΔE. The directional exposure is hereafter considered as independent of the right-ascension, as defined in section 4. Within an energy interval ΔE, the expected arrival direction distribution thus reads :

$$\frac{\mathrm{d}N(\mathbf{n})}{\mathrm{d}\Omega} \propto \tilde{\omega}(\delta) \sum_{\ell\geq 0} \sum_{m=-\ell}^{\ell} a_{\ell m} Y_{\ell m}(\mathbf{n}), \tag{18}$$

where $\tilde{\omega}(\delta)$ is the effective directional exposure for the energy interval ΔE. For convenience, this latter function is normalised such that :

$$\tilde{\omega}(\delta) = \frac{\displaystyle\int_{\Delta E} \mathrm{d}E\ E^{-\gamma}\omega(\delta, E)}{\displaystyle\max_{\delta}\left[\int_{\Delta E} \mathrm{d}E\ E^{-\gamma}\omega(\delta, E)\right]}, \tag{19}$$

with γ the spectral index in the considered energy range. This dimensionless function provides, for any direction on the sky, the effective directional exposure in the energy range ΔE at that direction, *relative* to the largest directional exposure on the sky. This is actually the relevant quantity which enters into Eqn. 14 for the analyses presented below. Note that for a directional exposure independent of the right ascension, the coefficients $[K]_{\ell m}^{\ell' m'}$ are proportional to $\delta_m^{m'}$ - *i.e.* different values of m are not mixed in the matrix. The observed arrival direction distribution, $\overline{\mathrm{d}N}(\mathbf{n})/\mathrm{d}\Omega$, is here modelled as a sum of Dirac functions on the sphere weighted by the factor $\Delta N_{\mathrm{cell}}^{-1}(\alpha_k^0)$ for each event recorded at local sidereal time α_k^0, as described in section 4.1 to correct for the slightly non-uniform directional exposure in right ascension. In this way, the integration in Eqn. 14 yields for the $b_{\ell m}$ coefficients to :

$$\overline{b}_{\ell m} = \sum_{k=1}^{N} \frac{Y_{\ell m}(\mathbf{n}_k)}{\Delta N_{\mathrm{cell}}(\alpha_k^0)}. \tag{20}$$

The multipolar coefficients $\overline{a}_{\ell m}$ are then recovered by means of Eqn. 16. Given the exposure functions described in section 4, the resolution on each recovered coefficient, encoded in Eqn. 17, is degraded by a factor larger than 2 each time ℓ_{max} is incremented by 1. This prevents the recovery of each coefficient with good accuracy as soon as $\ell_{\mathrm{max}} \geq 3$, since, for $\ell_{\mathrm{max}} = 3$ for instance, our current statistics would only allow us to probe dipole amplitudes at the 10% level. Consequently, in the following, we restrict ourselves to reporting results on individual coefficients obtained when assuming a dipolar distribution ($\ell_{\mathrm{max}} = 1$) and a quadrupolar distribution ($\ell_{\mathrm{max}} = 2$). Meanwhile, due to the interferences between modes induced by the non-uniform and partial sky coverage, it is important to stress again that each multipolar coefficient recovered under the assumption of a particular bound ℓ_{max} might be biased if the underlying angular distribution of cosmic rays is not bounded to $\ell_{\max}$. Given the directional exposure functions considered in this study, this effect can be important only if the angular distribution has in fact important moments of order $\ell_{\max}+1$.

5.2. Searches for dipolar patterns

As outlined in the introduction, a measurable dipole is regarded as a likely possibility in many scenarios of cosmic ray origins at EeV energies. Assuming that the angular distribution of cosmic rays is modulated by a *pure* dipole, the intensity $\Phi(\mathbf{n})$ can be parameterised in any direction $\mathbf{n}$ as :

$$\Phi(\mathbf{n}) = \frac{\Phi_0}{4\pi}\,\Big(1 + r\ \mathbf{d}\cdot\mathbf{n}\Big), \tag{21}$$

where $\mathbf{d}$ denotes the dipole unit vector. The dipole pattern is here fully characterised by a declination δ_d, a right ascension α_d, and an *amplitude* r corresponding to the maximal anisotropy contrast :

$$r = \frac{\Phi_{\max}-\Phi_{\min}}{\Phi_{\max}+\Phi_{\min}}. \tag{22}$$

The estimation of these three coefficients is straightforward from the estimated spherical harmonic coefficients $\overline{a}_{1m}$: $\overline{r} = [3(\overline{a}_{10}^2+\overline{a}_{11}^2+\overline{a}_{1-1}^2)]^{0.5}/\overline{a}_{00}$, $\overline{\delta} = \arcsin\big(\sqrt{3}\overline{a}_{10}/\overline{a}_{00}\overline{r}\big)$, and $\overline{\alpha} = \arctan\big(\overline{a}_{1-1}/\overline{a}_{11}\big)$. Uncertainties on $\overline{r}$, $\overline{\delta}$ and $\overline{\alpha}$ are obtained from the propagation of uncertainties on each recovered $\overline{a}_{1m}$ coefficient (*cf* Eqn. 17). Under an underlying isotropic distribution, and for an axisymmetric directional exposure around the axis defined by the North and South equatorial poles, the probability density function of $\overline{r}$ is given by (Pierre Auger Collaboration 2011b) :

$$p_R(\overline{r}) = \frac{\overline{r}}{\sigma\sqrt{\sigma_z^2-\sigma^2}}\ \mathrm{erfi}\bigg(\frac{\sqrt{\sigma_z^2-\sigma^2}}{\sigma\sigma_z}\frac{\overline{r}}{\sqrt{2}}\bigg)\ \exp\bigg(-\frac{\overline{r}^2}{2\sigma^2}\bigg), \tag{23}$$

where $\mathrm{erfi}(z)=\mathrm{erf}(iz)/i$, $\sigma=\sqrt{3}\sigma_{11}/\overline{a}_{00}$, and $\sigma_z=\sqrt{3}\sigma_{10}/\overline{a}_{00}$. The probability $P_R(>\overline{r})$ that an amplitude equal or larger than $\overline{r}$ arises from a statistical fluctuation of an isotropic distribution is then obtained by integrating p_R above $\overline{r}$:

$$P_R(>\overline{r}) = \mathrm{erfc}\bigg(\frac{\overline{r}}{\sqrt{2}\sigma_z}\bigg) + \mathrm{erfi}\bigg(\frac{\sqrt{\sigma_z^2-\sigma^2}}{\sigma\sigma_z}\frac{\overline{r}}{\sqrt{2}}\bigg)\ \exp\bigg(-\frac{\overline{r}^2}{2\sigma^2}\bigg). \tag{24}$$

The reconstructed amplitudes $\overline{r}(E)$ and corresponding directions are shown in Fig. 5 with the associated uncertainties, as a function of the energy. The directions are drawn in azimuthal projection, with the equatorial South pole located at the centre and the right-ascension going from 0 to 360° clockwise. In the

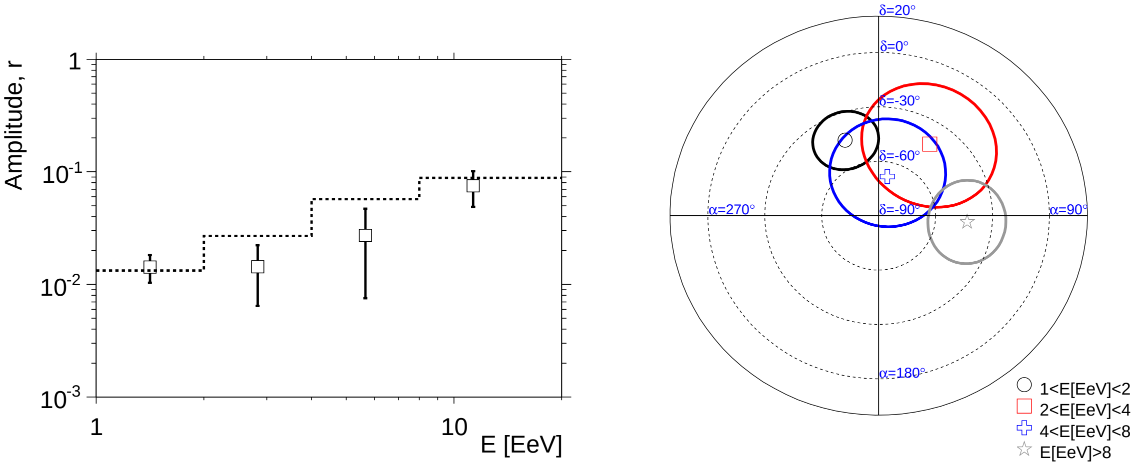

Fig. 5.— Left : Reconstructed amplitude of the dipole as a function of energy. The dotted line stands for the 99% $C.L.$ upper bounds on the amplitudes that would result from fluctuations of an isotropic distribution. Right : Reconstructed declination and right-ascension of the dipole with corresponding uncertainties, as a function of energy, in azimuthal projection.

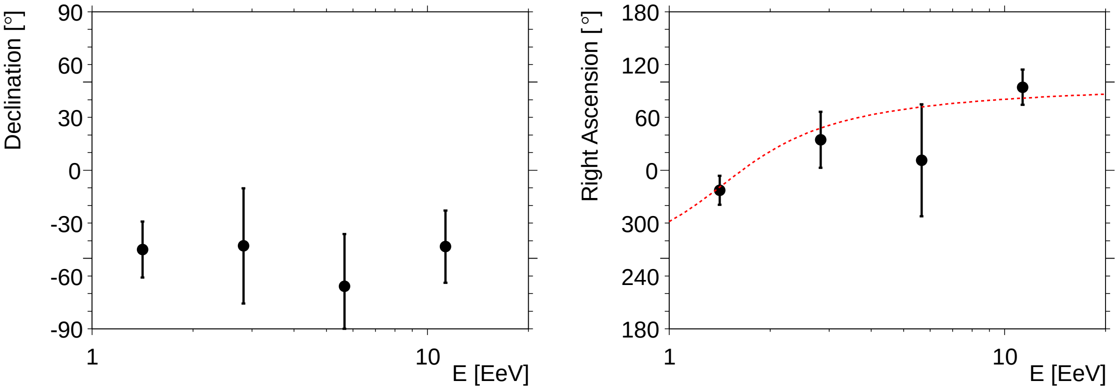

Fig. 6.— Reconstructed declination (left) and right ascension (right) of the dipole as a function of energy. The smooth fit to the data of (Pierre Auger Collaboration 2011a) is shown as the dashed line in the right panel : a consistent smooth behaviour is observed using the analysis presented here and applied to a data set containing two additional years of data.

left panel, the 99% $C.L.$ upper bounds on the amplitudes that would result from fluctuations of an isotropic distribution are indicated by the dotted line ($i.e.$ the amplitudes $\overline{r}_{99}(E)$ such that $P_R(>\overline{r}_{99}(E)) = 0.01$).

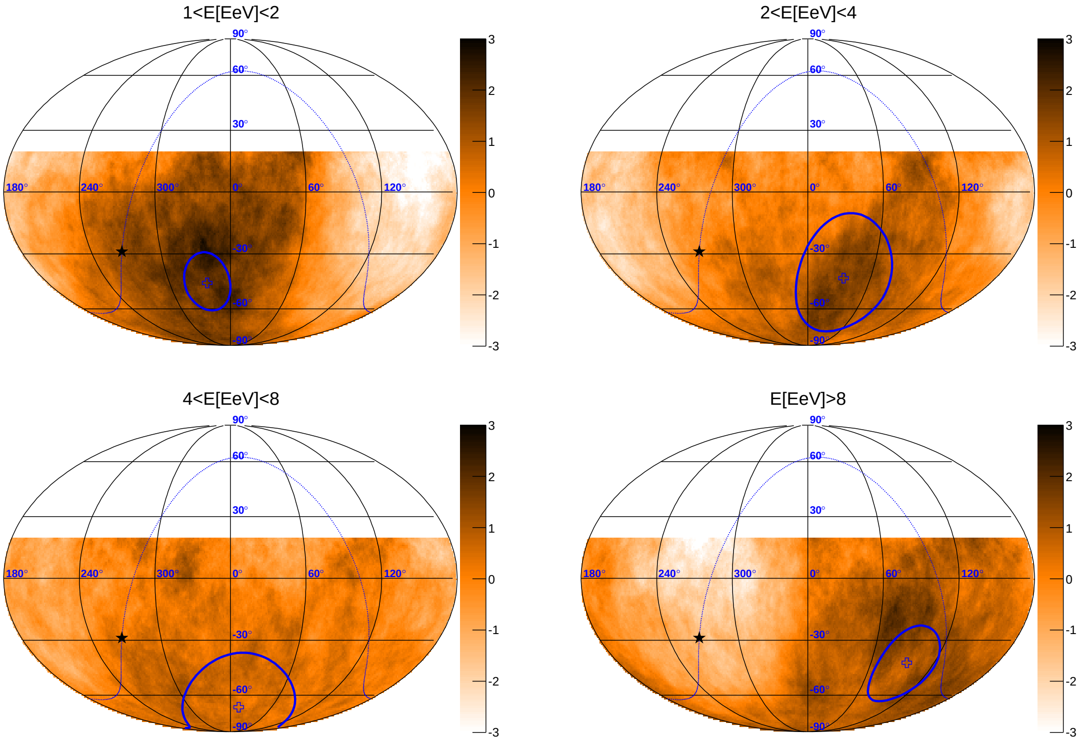

1<E[EeV]<2

2<E[EeV]<4

4<E[EeV]<8

E[EeV]>8

Fig. 7.— Significance sky maps in four independent energy bins. The maps are smoothed using an angular window with radius $\Theta = 1$ radian, to exhibit any dipolar-like structures. The directions of the reconstructed dipoles are shown with the associated uncertainties. The galactic plane and galactic center are also depicted as the dotted line and the star.

One can see that within the statistical uncertainties, there is no strong evidence of any significant signal.

The reconstructed declinations $\overline{\delta}$ and right ascensions $\overline{\alpha}$ are shown separately in Fig 6. Both quantities are expected to be randomly distributed in case of independent samples whose parent distribution is isotropic. In our previous report on first harmonic analysis in right ascension (Pierre Auger Collaboration 2011a), we pointed out the intriguing smooth alignment of the phases in right ascension as a function of the energy, and noted that such a consistency of phases in adjacent energy intervals is expected with smaller number of events than the detection of amplitudes standing-out significantly above the background noise in case of a real underlying anisotropy. This motivated us to design a *prescription* aimed at establishing at 99% *C.L.* whether this consistency in phases is real, using the exact same analysis as the one reported in Ref (Pierre Auger Collaboration 2011a). The prescription will end once the total exposure since 25 June

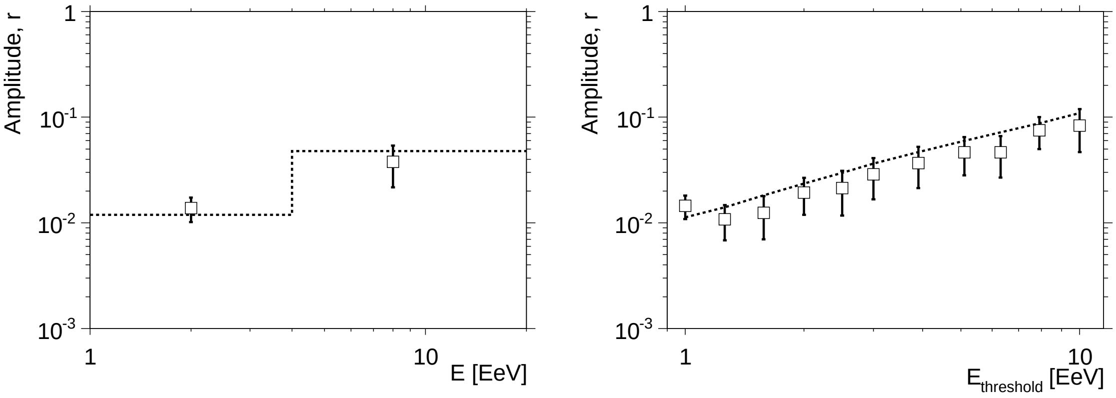

Fig. 8.— Left : Amplitude of the dipole for two energy intervals : $1 < E/[\mathrm{EeV}] < 4$ and $E > 4$ EeV. Right : Amplitude of the dipole as a function of energy thresholds. The dotted lines stand for the 99% *C.L.* upper bounds on the amplitudes that could result from fluctuations of an isotropic distribution.

2011 reaches 21,000 km^2 yr sr. The smooth fit to the data of Ref (Pierre Auger Collaboration 2011a) is shown as a dashed line in the right panel of Fig 6, restricted to the energy range considered here. Though the phase between 4 and 8 EeV is poorly determined due to the corresponding direction in declination pointing close to the equatorial south pole, it is noteworthy that a consistent smooth behaviour is observed using the analysis presented here and applied to a data set containing two additional years of data. It is also interesting to see in the left panel that all reconstructed declinations are in the equatorial southern hemisphere.

For completeness, significance sky maps are displayed in Fig. 7 in equatorial coordinates and using a Mollweide projection, for the four energy ranges. The galactic plane and galactic center are also depicted as the dotted line and the star. Significances are calculated using the Li and Ma estimator (Li & Ma 1983). The maps show the overdensities obtained in circular windows of radius $\Theta = 1$ radian, to better exhibit possible dipolar-like structures. The directions of the reconstructed dipoles are also shown, with their associated uncertainties (thick circles).

Finally, since some consistency is observed both in declination and right ascension as a function of energy, the use of larger energy intervals and/or energy thresholds may help to pick up a significant signal above the background level. The amplitudes of the dipole are shown in Fig. 8 for two energy intervals ($1 < E/[\mathrm{EeV}] < 4$ and $E > 4$ EeV) and as a function of energy thresholds. This does not provide any further evidence for significant anisotropies.

5.3. Searches for quadrupolar patterns

Any excesses along a plane would show up as a prominent quadrupole moment. Such excesses are plausible for instance at EeV energies in case of an emission of light EeV-cosmic rays from sources preferentially located in the galactic disk, or at higher energies from sources preferentially located in the super-galactic plane. Consequently, a measurable quadrupole may be regarded as an interesting outcome of an anisotropy search at ultra high energies.

Assuming now that the angular distribution of cosmic rays is modulated by a dipole *and* a quadrupole, the intensity $\Phi(\mathbf{n})$ can be parameterised in any direction $\mathbf{n}$ as :

$$\Phi(\mathbf{n}) = \frac{\Phi_0}{4\pi}\left(1 + r\ \mathbf{d}\cdot\mathbf{n} + \frac{1}{2}\sum_{i,j} Q_{ij}n_in_j\right), \tag{25}$$

where $\mathbf{Q}$ is a traceless and symmetric second order tensor. Its five independent components are determined in a straightforward way from the $\ell = 2$ spherical harmonic coefficients a_{2m}. Denoting by $\lambda_+, \lambda_0, \lambda_-$ the three eigenvalues of $\mathbf{Q}/2$ (λ_+ being the highest one and λ_- the lowest one) and $\mathbf{q}_+, \mathbf{q_0}, \mathbf{q}_-$ the three corresponding unit eigenvectors, the intensity can be parameterised in a more intuitive way as :

$$\Phi(\mathbf{n}) = \frac{\Phi_0}{4\pi}\left(1 + r\ \mathbf{d}\cdot\mathbf{n} + \lambda_+(\mathbf{q}_+\cdot\mathbf{n})^2 + \lambda_0(\mathbf{q_0}\cdot\mathbf{n})^2 + \lambda_-(\mathbf{q}_-\cdot\mathbf{n})^2\right). \tag{26}$$

It is then convenient to define the quadrupole amplitude β as :

$$\beta = \frac{\lambda_+ - \lambda_-}{2 + \lambda_+ + \lambda_-}. \tag{27}$$

In case of a pure quadrupolar distribution (*i.e.* in the absence of dipole), β is nothing else but the customary measure of maximal anisotropy contrast :

$$r = 0 \Rightarrow \beta = \frac{\lambda_+ - \lambda_-}{2 + \lambda_+ + \lambda_-} = \frac{\Phi_{\max} - \Phi_{\min}}{\Phi_{\max} + \Phi_{\min}}. \tag{28}$$

Hence, any quadrupolar pattern can be fully described by two amplitudes (β, λ_+) and three angles : (δ_+, α_+) which define the orientation of $\mathbf{q}_+$ and (α_-) which defines the direction of $\mathbf{q}_-$ in the orthogonal plane to $\mathbf{q}_+$. The third eigenvector $\mathbf{q_0}$ is orthogonal to $\mathbf{q}_+$ and $\mathbf{q}_-$, and its corresponding eigenvalue λ_0 is such that the traceless condition is satisfied : $\lambda_+ + \lambda_- + \lambda_0 = 0$. Though the probability density functions of the estimated quadrupole amplitudes $(\overline{\beta}, \overline{\lambda}_+)$ can be in principle calculated in the same way as

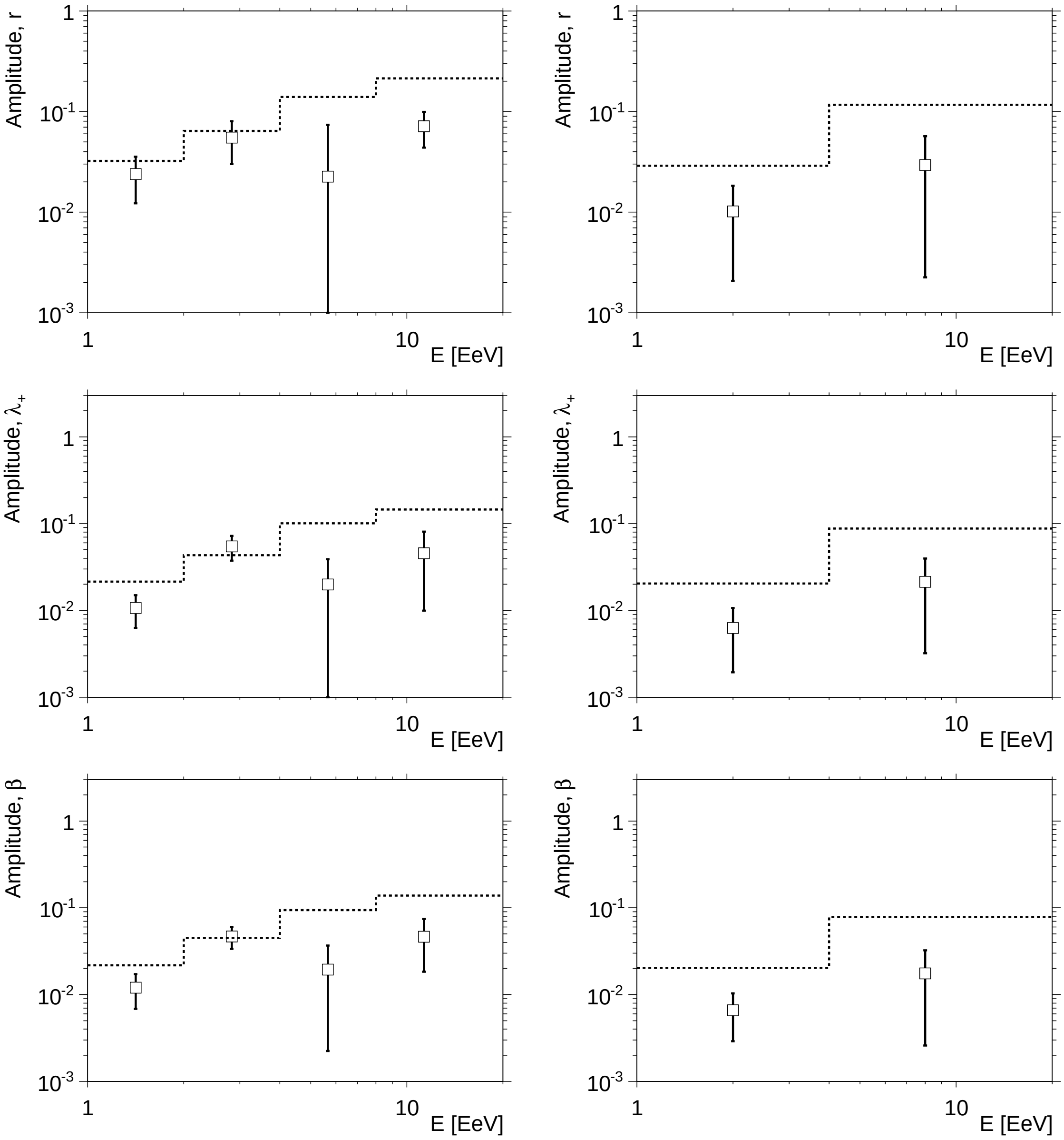

Fig. 9.— Amplitudes of the dipolar (top) and quadrupolar moments (middle and bottom) as a function of energy using a multipolar reconstruction up to $\ell_{\max} = 2$, for two different binnings (left and right). In each panel, the dotted lines stand for the 99% *C.L.* upper bounds on the amplitudes that could result from fluctuations of an isotropic distribution.

in the case of the estimated dipole amplitude ($\overline{r}$), expressions are much more complicated to obtain even semi-analytically and we defer hereafter to Monte-Carlo simulations to tabulate the distributions.

The amplitudes $\overline{r}(E)$, $\overline{\lambda}_+(E)$ and $\overline{\beta}(E)$ are shown in Fig. 9 as functions of energy. Dipole amplitudes are compatible with expectations from isotropy. Compared to the results on the dipole obtained in previous section for $\ell_{\mathrm{max}} = 1$, the sensitivity is now degraded by a factor larger than 2 as expected from the dependence of the resolution $\sigma_{\ell m}$ on ℓ_{max} (*cf* Eqn. 17). In the same way as for dipole amplitudes, the 99% *C.L.* upper bounds on the quadrupole amplitudes that could result from fluctuations of an isotropic distribution are indicated by the dashed lines. They correspond to the amplitudes $\overline{\lambda}_{+,99}(E)$ and $\overline{\beta}_{99}(E)$ such that the probabilities $P_{\Lambda_+}(> \overline{\lambda}_{+,99}(E))$ and $P_B(> \overline{\beta}_{99}(E))$ arising from statistical fluctuations of isotropy are equal to 0.01. Here, both distributions P_{Λ_+} and P_B are sampled from Monte-Carlo simulations. Throughout the energy scan, there is no evidence for anisotropy. The largest deviation from isotropic expectations occurs between 2 and 4 EeV, where both amplitudes $\overline{\lambda}_+$ and $\overline{\beta}$ lie just above $\overline{\lambda}_{+99}$ and $\overline{\beta}_{99}$.

6. Additional cross-checks against experimental effects

6.1. More on the influence of shower size corrections for geomagnetic effects

Understanding the influence of the shower size corrections for geomagnetic effects is critical to get unbiased estimates of anisotropy parameters. Without accounting for these effects, an increase of the event rate would be observed close to the equatorial South pole with respect to expectations for isotropy, while a decrease would be observed close to the edge of the directional exposure in the equatorial Northern hemisphere. This would result in the observation of a fake dipole. A convenient way to exhibit this effect is to separate the dipole in two components : the component of the dipole in the equatorial plane $r_\perp$, and the component along the Earth rotation axis, $r_\parallel$. While $r_\perp$ is expected to be affected only by any time-dependent effect, $r_\parallel$ is on the flip side the relevant quantity sensitive to time-independent effects such as the geomagnetic one.

ΔE [EeV]	$\overline{r}_\perp^{uncorr}[\%]$	$\overline{r}_\perp[\%]$	$\overline{r}_\parallel^{uncorr}[\%]$	$\overline{r}_\parallel[\%]$
$1-4$	0.9 ± 0.3	0.9 ± 0.3	-2.2 ± 0.4	-1.0 ± 0.4
> 4	1.8 ± 1.0	2.1 ± 1.0	-4.1 ± 1.7	-3.0 ± 1.7

Table 2: Influence of shower size corrections for geomagnetic effects on the component of the dipole in the equatorial plane and on the one along the Earth rotation axis.

Estimations of $r_\perp$ and $r_\parallel$ obtained by accounting or not for geomagnetic effects are given in Table 2, in two different energy ranges. These estimations are obtained from the recovered $\overline{a}_{1m}$ coefficients : $\overline{r}_\parallel = \sqrt{3}\overline{a}_{10}/\overline{a}_{00}$, and $\overline{r}_\perp = [3(\overline{a}_{11}^2 + \overline{a}_{1-1}^2]^{0.5}/\overline{a}_{00}$. It can be seen that the main effect of the geomagnetic corrections is a shift in $\overline{r}_\parallel$ of about 1.2%. In the energy range $1 \leq E/[\mathrm{EeV}] \leq 4$, this shift is significant, $\overline{r}_\parallel$ changing from -2.2% to -1.0% with an uncertainty amounting to 0.4%. Above 4 EeV, the net correction is of the same order, though the statistical uncertainties are larger. In contrast, $\overline{r}_\perp$ remains unchanged in both cases, as expected.

6.2. Eventual energy dependence of the attenuation curve

In this section, we study in which extent the procedure used to obtain the attenuation curve in section 3.3 might influence the determination of anisotropy parameters.

To convert the shower size into energy, we explained and applied in section 3.3 the constant intensity cut method for showers with $S_{38^\circ} \geq 22$ VEM, that is, just above the threshold energy for full efficiency. The value of the parameter a obtained in these conditions is consistent within the statistical uncertainties with the one previously reported when applying the same constant intensity cut method for showers with $S_{38^\circ} \geq 47$ VEM. Opposite to this, the value obtained for the coefficient b differs by more than 3 standard deviations. Such a difference might be expected from both the evolution of the maximum of the showers and from an eventual change in composition with energy, but it may also be due to energy and angle-dependent resolutions effects mimicking a real evolution with energy.

With a different attenuation curve, some events would be reconstructed in the adjacent energy intervals in an extent which depends on the change of the attenuation curve with zenith angle. For that reason, the determination of anisotropy parameters might be altered by this effect.

Disentangling real evolution of the attenuation curve with energy from resolution effects is out of the scope of this paper and will be addressed elsewhere. Here, we restrict ourselves to probe the effect that a real energy dependence would have on the determination of anisotropy parameters. To do so, we choose to fit the values of the coefficient b obtained for $S_{38^\circ} = 22$ VEM and $S_{38^\circ} = 47$ VEM through a linear dependence with the logarithm of S_{38°. Below and above these values, the behaviour of $b(E)$ is obtained by *extrapolating* this energy dependence. In this way, the changes in the anisotropy parameters are probed in *extreme* conditions.

Repeating the whole chain of analysis with this new attenuation curve, it turns out that the reconstructed dipole parameters are only marginally affected by this change, as illustrated in the top and middle panels of Fig. 10. Meanwhile, both reconstructed quadrupole amplitudes in the energy interval $2 \leq E/\mathrm{EeV} \leq 4$ are reduced in such a way that they lie now below the 99% upper bounds for isotropy. Conversely, the amplitudes in the energy interval $1 \leq E/\mathrm{EeV} \leq 2$ are increased so that they lie now above the 99% upper bounds for isotropy. Below 4 EeV, the determination of the attenuation curve thus appears to be the main source of systematic uncertainties for determining the quadrupole amplitudes. The two extreme extrapolations performed in this analysis (*i.e.* b constant with the energy or linearly dependent with the logarithm of the energy) allows us to bracket the possible values.

6.3. Systematic uncertainties associated to corrections for weather and geomagnetic effects

In section 3, we presented the procedure adopted to account for the changes in shower size due to weather and geomagnetic effects. Since the coefficients α_P, α_ρ and β_ρ in Eqn. 1 were extracted from real data, they suffer from statistical uncertainties which may impact in a systematic way the corrections made on $S(1000)$, and consequently may also impact the anisotropy parameters derived from the data set. Besides, the determination of g_1 and g_2 in Eqn. 2 is based on the simulation of showers. Both the systematic uncertainties associated to the different interaction models and primary masses and the statistical uncertainties related to the procedure used to extract g_1 and g_2 constitute a source of systematic uncertainties on the anisotropy parameters.

To quantify these systematic uncertainties, we repeated the whole chain of analysis on a large number of modified data sets. Each modified data set is built by sampling randomly the coefficients α_P, α_ρ and β_ρ (or g_1 and g_2 when dealing with geomagnetic effects) according to the corresponding uncertainties and correlations between parameters through the use of a Gaussian probability distribution function. For each new set of correction coefficients, new sets of anisotropy parameters are then obtained. The RMS of each resulting distribution for each anisotropy parameter is the systematic uncertainty that we assign. Results are shown in Fig. 10, in terms of the dipole and quadrupole amplitudes as a function of the energy. Balanced against the statistical uncertainties in the original analysis (shown by the bands), it is apparent that both sources of systematic uncertainties have a negligible impact on each reconstructed anisotropy amplitude.

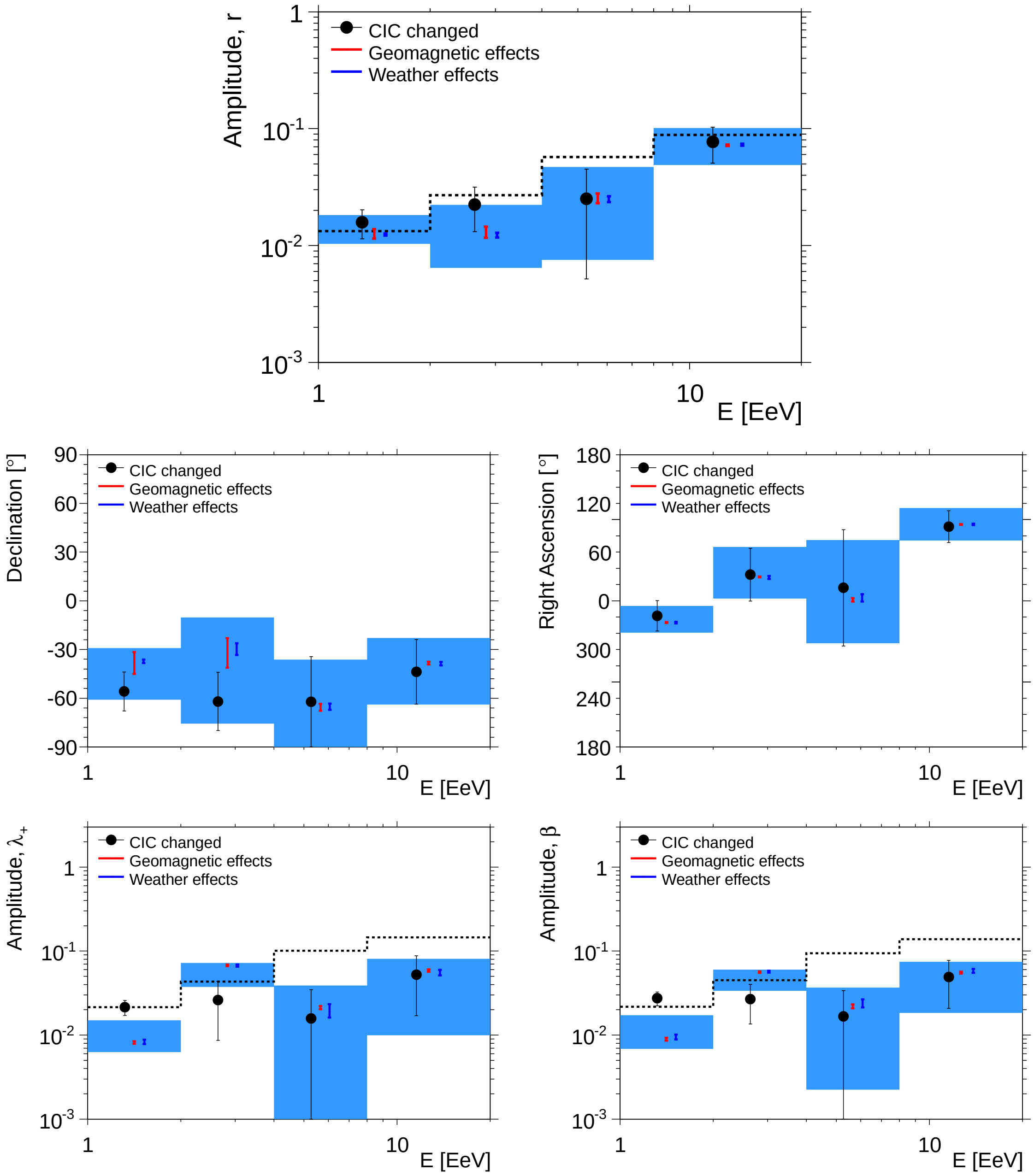

Fig. 10.— Impact of different sources of systematic uncertainties on the dipole amplitudes (top) and the dipole directions and phases (middle) obtained under the assumption $\ell_{\max} = 1$, and quadrupole amplitudes (bottom) obtained with $\ell_{\max} = 2$, as a function of the energy. The blue bands correspond to the results presented in Fig. 5 and Fig. 9.

7. Upper limits and discussion

From the analyses reported in section 5, upper limits on dipole and quadrupole amplitudes can be derived at 99% *C.L.* (see appendices C and D). All relevant results are summarised in Table 3 and Table 4. The upper limits are also shown in Fig. 11 accounting for the systematic uncertainties discussed in the previous section : in the two last energy bins, any of the systematic measurements yield to the same upper limit because all amplitudes lie well within the background noise. We illustrate below the astrophysical interest of these upper limits by calculating the amplitudes of anisotropy expected in a toy scenario in which sources of EeV-cosmic rays are stationary, densely and uniformly distributed in the galactic disk, and emit particles in all directions.

ΔE [EeV]	N	$\overline{r}$ [%]	$\overline{\delta}[^\circ]$	$\overline{\alpha}[^\circ]$	UL [%]
$1-2$	361260	1.4 ± 0.4	-45 ± 16	337 ± 16	1.8
$2-4$	88438	1.4 ± 0.8	-43 ± 32	34 ± 32	2.7
$4-8$	19861	2.7 ± 2.0	-66 ± 30	12 ± 63	5.8
> 8	8409	7.5 ± 2.6	-43 ± 20	94 ± 20	11.4

Table 3: Summary of the dipolar analysis ($\ell_{\max} = 1$) reported in section 5.2, together with the derived 99% *C.L.* upper limits (UL) on the amplitudes.

ΔE [EeV]	$\overline{\lambda}_+$ [%]	$\overline{\beta}$ [%]	UL (λ_+) [%]	UL (β) [%]
$1-2$	1.1 ± 0.4	1.2 ± 0.5	2.1	2.1
$2-4$	5.4 ± 1.8	4.7 ± 1.3	7.1	6.8
$4-8$	2.0 ± 1.9	1.9 ± 1.7	10.0	9.4
> 8	4.5 ± 3.6	4.7 ± 2.8	14.5	13.8

Table 4: Summary of the quadrupolar analysis ($\ell_{\max} = 2$) reported in section 5.3, together with the derived 99% *C.L.* upper limits (UL) on the amplitudes.

Both the strength and the structure of the magnetic field in the Galaxy, still remaining poorly known, play a crucial role in the propagation of cosmic rays. The field is thought to contain a large scale regular component and a small scale turbulent one, both having a local strength of a few microgauss (see *e.g.* (Beck 2001)). While the turbulent component dominates in strength by a factor of a few, the regular component imprints dominant drift motions as soon as the Larmor radius of cosmic rays is larger than the maximal scale of the turbulences (thought to be in the range 10-100 pc). We adopt in the following a recent parameterisation of the regular component obtained by fitting model field geometries to Faraday rotation measures of extragalactic radio sources and polarised synchrotron emission (Pshirkov *et al.* 2011). It consists in two different components : a disk field and a halo field. The disk field is symmetric with respect to the galactic plane, and is described by the widely-used logarithmic spiral model with reversal direction of the field in two different arms (the so-called *BSS-model*). The halo field is anti-symmetric with respect to the galactic plane and purely toroidal. The detailed parameterisation is given in Ref. (Pshirkov *et al.* 2011) (with the set of parameters reported in Table 3). In addition to the regular component, a turbulent field is generated according to a Kolmogorov power spectrum and is pre-computed on a three dimensional grid periodically repeated in space. The size of the grid is taken as 100 pc, so as the maximal scale of turbulences, and the strength of the turbulent component is taken as three times the strength of the regular one.

To describe the propagation of cosmic rays with energies $E \geq 1$ EeV in such a magnetic field, the direct integration of trajectories is the most appropriate tool. Performing the forward tracking of particles from galactic sources and recording those particles which cross the Earth is however not feasible within a reasonable computing time. So, to obtain the anisotropy of cosmic rays emitted from sources uniformly distributed in a disk with a radius of 20 kpc from the galactic centre and with a height of ± 100 pc, we adopt a method first proposed in Ref. (Thielheim & Langhoff 1968) and then widely used in the literature. It consists in back tracking anti-particles with random directions from the Earth to outside the Galaxy. Each test particle *probes* the total luminosity along the path of propagation from each direction as seen from the Earth. For *stationary sources emitting cosmic rays in all directions*, the time spent by each test particle in the source region is then proportional to the flux detected in the initial sampled direction.

The amplitudes of anisotropy obviously depend on the rigidity E/Z of the cosmic rays, with Z the electric charge of the particles. Since we only aim at illustrating the upper limits, we consider two extreme single primaries : protons and iron nuclei. In the energy range $1 \leq E/\mathrm{EeV} \leq 20$, it is unlikely that our measurements on the average position in the atmosphere of the shower maximum and the corresponding RMS can be reproduced with a single primary (Pierre Auger Collaboration 2010c). As well, in the scenario explored here and for a single primary, the energy spectrum is expected to reveal a *hardening*

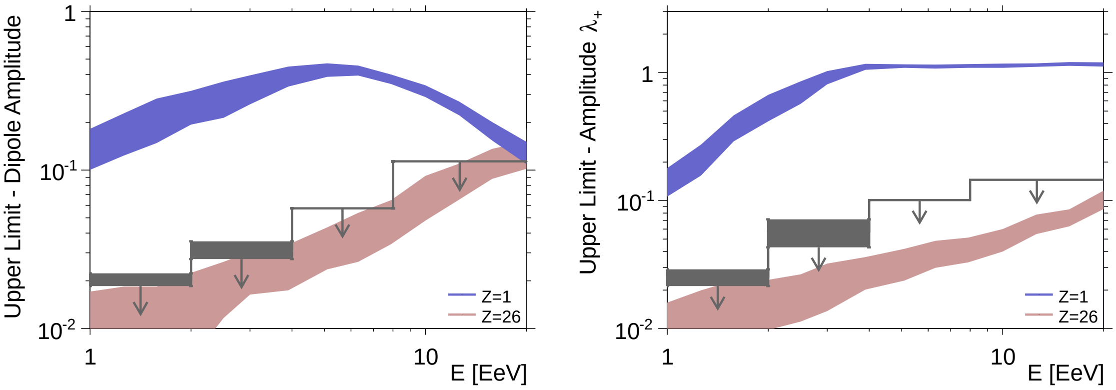

Fig. 11.— 99% *C.L.* upper limits on dipole and quadrupole amplitudes as a function of the energy. Some generic anisotropy expectations from stationary galactic sources distributed in the disk are also shown, for various assumptions on the cosmic ray composition. The fluctuations of the amplitudes due to the stochastic nature of the turbulent component of the magnetic field are sampled from different simulation data sets and are shown by the bands (see text).

in this energy range, whose origin is from the one expected if the ankle marks the cross-over between galactic and extragalactic cosmic rays (Linsley 1963) or if it marks the distortion of a proton-dominated extragalactic spectrum due to e^+/e^- pair production of protons with the photons of the cosmic microwave background (Hillas 1967; Blumenthal 1970; Berezinsky *et al.* 2006; Berezinsky *et al.* 2004). For a given configuration of the magnetic field, the exact energy at which this hardening occurs depends on the electric charge of the cosmic rays. This is because the average time spent in the source region first decreases as $\simeq E^{-1}$ and then tends to the constant free escape time as a consequence of the direct escape from the Galaxy. The hardening with $\Delta\gamma \simeq 0.6$ observed at 4 EeV in our measurements of the energy spectrum is not compatible with the one expected in this scenario ($\Delta\gamma \simeq 1$). Nevertheless, the calculation of dipole and quadrupole amplitudes for single primaries is useful to probe the allowed contribution of each primary as a function of the energy.

The dipole and quadrupole λ_+ amplitudes obtained for several energy values covering the range $1 \leq E/\mathrm{EeV} \leq 20$ are shown in Fig. 11. To probe unambiguously amplitudes down to the percent level, it is necessary to generate simulated event sets with $\simeq 5\ 10^5$ test particles. Such a number of simulated events allows us to shrink statistical uncertainties on amplitudes at the 0.5% level. Meanwhile, there is an intrinsic variance in the model for each anisotropy parameter due to the stochastic nature of the turbulent component of the magnetic field. This variance is estimated through the simulation of 20 sets of 5 10^5 test particles, where the configuration of the turbulent component is frozen in each set. The RMS of the amplitudes sampled in this way is shown by the bands in Fig. 11. While the dipole amplitude steadily increases for iron nuclei, this is not the case any longer for protons around the ankle energy. This is because we explore a source region uniformly distributed in the disk. Consequently, the image of the galactic plane appears less distorted by the magnetic field with increasing energy. This gives rise to an important quadrupolar moment which actually turns out to be the main feature of the anisotropy at large scale [6].

The dipole and quadrupole λ_+ amplitudes obtained here depend on the model used to describe the galactic magnetic field. We note that recently, a new model was given in Ref (Farrar & Jansson 2012), providing improved fits to Faraday rotation measures of extragalactic radio sources and polarised synchrotron emission observations. However, we tested at a few energies that the results obtained are qualitatively in agreement with the ones presented in Fig. 11. Similar conclusions were given in Ref (Giacinti *et al.* 2011), where more systematic studies can be found in terms of the field strength and geometry.

Around 1 EeV, there is evidence that the cosmic ray composition includes a strong light component (Pierre Auger Collaboration 2010c). It is apparent that amplitudes derived for protons largely stand above the allowed limits. Consequently, unless the strength of the magnetic field is much higher than in the picture used here, the upper limits derived in this analysis exclude that the light component of cosmic rays comes from galactic stationary sources densely distributed in the galactic disk and emitting in all directions. This is in agreement with the absence of any detectable point-like sources above 1 EeV that would be indicative of a flux of neutrons produced by EeV-protons through mainly pion-producing interactions in the source environments (Pierre Auger Collaboration 2012b). On the other hand, if the measurements of the cosmic ray composition around 1 EeV result from a mixture containing a large fraction of iron nuclei of galactic origin, upper limits can still be respected, or alternatively a light component of extragalactic origin would be allowed. Future measurements of composition below 1 EeV will come from the low energy extension HEAT now available at the Pierre Auger Observatory (Mathes *et al.* 2011). Combining these measurements with large scale anisotropy ones will then allow us to further understand the origin of cosmic rays at energies less than 4 EeV.

---

[6] This feature would remain in the case of a radial distribution of sources following the matter in the Galaxy, though the dipole amplitude would steadily increase above the ankle energy.

8. Summary

For the first time, a thorough search for large scale anisotropies as a function of both the declination and the right ascension in the distribution of arrival directions of cosmic rays detected above 1 EeV at the Pierre Auger Observatory has been presented. With respect to the traditional search in right ascension only, this search requires the control of additional systematic effects affecting both the exposure of the sky and the counting rate of events in local angles. All these effects were carefully accounted for and presented in sections 3 and 4. No significant deviation from isotropy is revealed within the systematic uncertainties, although the consistency in the dipole phases may be indicative of a genuine signal whose amplitude is at the level of the statistical noise. The sensitivity accumulated so far to dipole and quadrupole amplitudes allows us to challenge an origin of cosmic rays from stationary galactic sources densely distributed in the galactic disk and emitting predominantly light particles in all directions.

Future work will profit from both the increased statistics and the lower energy threshold that is now available at the Pierre Auger Observatory (Mathes *et al.* 2011; Sanchez *et al.* 2011). This will provide further constraints helping to understand the origin of cosmic rays in the energy range $0.1 < E/\text{EeV} < 10$.

Acknowledgements

The successful installation, commissioning, and operation of the Pierre Auger Observatory would not have been possible without the strong commitment and effort from the technical and administrative staff in Malargüe.

We are very grateful to the following agencies and organizations for financial support: Comisión Nacional de Energía Atómica, Fundación Antorchas, Gobierno De La Provincia de Mendoza, Municipalidad de Malargüe, NDM Holdings and Valle Las Leñas, in gratitude for their continuing cooperation over land access, Argentina; the Australian Research Council; Conselho Nacional de Desenvolvimento Científico e Tecnológico (CNPq), Financiadora de Estudos e Projetos (FINEP), Fundação de Amparo à Pesquisa do Estado de Rio de Janeiro (FAPERJ), Fundação de Amparo à Pesquisa do Estado de São Paulo (FAPESP), Ministério de Ciência e Tecnologia (MCT), Brazil; AVCR AV0Z10100502 and AV0Z10100522, GAAV KJB100100904, MSMT-CR LA08016, LG11044, MEB111003, MSM0021620859, LA08015 and TACR TA01010517, Czech Republic; Centre de Calcul IN2P3/CNRS, Centre National de la Recherche Scientifique (CNRS), Conseil Régional Ile-de-France, Département Physique Nucléaire et Corpusculaire (PNC-IN2P3/CNRS), Département Sciences de l'Univers (SDU-INSU/CNRS), France; Bundesministerium für Bildung und Forschung (BMBF), Deutsche Forschungsgemeinschaft (DFG), Finanzministerium Baden-Württemberg, Helmholtz-Gemeinschaft Deutscher Forschungszentren (HGF), Ministerium für Wissenschaft und Forschung, Nordrhein-Westfalen, Ministerium für Wissenschaft, Forschung und Kunst, Baden-Württemberg, Germany; Istituto Nazionale di Fisica Nucleare (INFN), Ministero dell'Istruzione, dell'Università e della Ricerca (MIUR), Italy; Consejo Nacional de Ciencia y Tecnología (CONACYT), Mexico; Ministerie van Onderwijs, Cultuur en Wetenschap, Nederlandse Organisatie voor Wetenschappelijk Onderzoek (NWO), Stichting voor Fundamenteel Onderzoek der Materie (FOM), Netherlands; Ministry of Science and Higher Education, Grant Nos. N N202 200239 and N N202 207238, Poland; Portuguese national funds and FEDER funds within COMPETE - Programa Operacional Factores de Competitividade through Fundação para a Ciência e a Tecnologia, Portugal; Romanian Authority for Scientific Reseach, UEFICDI, Ctr.Nr.1/ASPERA2 ERA-NET, Romania; Ministry for Higher Education, Science, and Technology, Slovenian Research Agency, Slovenia; Comunidad de Madrid, FEDER funds, Ministerio de Ciencia e Innovación and Consolider-Ingenio 2010 (CPAN), Xunta de Galicia, Spain; Science and Technology Facilities Council, United Kingdom; Department of Energy, Contract Nos. DE-AC02-07CH11359, DE-FR02-04ER41300, National Science Foundation, Grant No. 0450696, The Grainger Foundation USA; NAFOSTED, Vietnam; Marie Curie-IRSES/EPLANET, European Particle Physics Latin American Network, European Union 7th Framework Program, Grant No. PIRSES-2009-GA-246806; and UNESCO.

Appendix A : Large scale anisotropies in local coordinates

To study the angular distribution in local coordinates for different anisotropic angular distributions $\Phi(\alpha,\delta)$ in celestial coordinates, we restrict ourselves, without loss of generalities, to the case of full detection efficiency ($\epsilon(\theta,\varphi,E)=1$). Then, the instantaneous arrival direction distribution in local coordinates reads :

$$\frac{\mathrm{d}^3N}{\mathrm{d}\theta\mathrm{d}\varphi\mathrm{d}\alpha^0}\propto\sin\theta\;\cos\theta\;\Phi(\theta,\varphi,\alpha^0). \tag{29}$$

$\Phi(\theta,\varphi,\alpha^0)$ is the underlying angular distribution of cosmic rays, expressed in local coordinates. In case of isotropy, Φ is constant so that once integrated over φ and α^0, the arrival direction distribution is such that $\mathrm{d}N/\mathrm{d}\sin^2\theta$ is also constant. On the other hand, in case of a dipolar distribution for instance, Φ is proportional to $1+r\mathbf{d}(\theta,\varphi,\alpha^0)\cdot\mathbf{n}(\theta,\varphi)$, where $\mathbf{n}$ is here a unit vector in local coordinates, and $\mathbf{d}$ the dipole unit vector pointing towards (α_d,δ_d) and expressed in local coordinates by means of Eqn. 4. To quantify

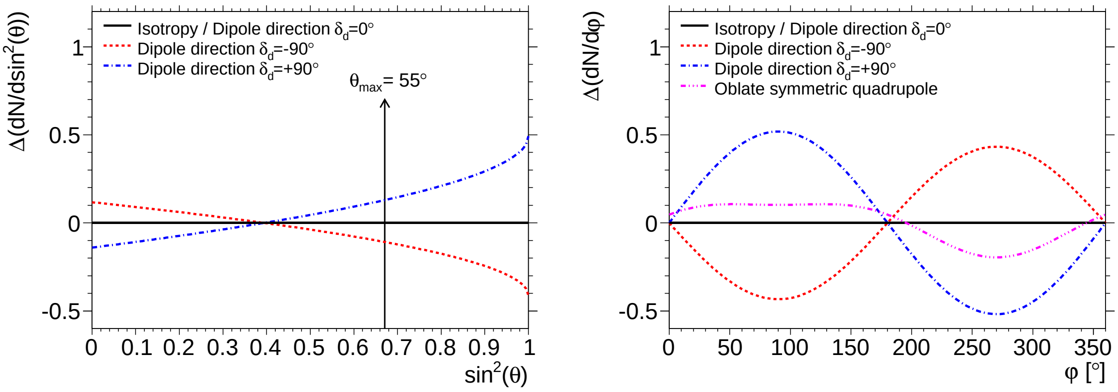

Fig. 12.— Effect of large scale anisotropies in local coordinates (left : as a function of $\sin^2\theta$, right : as a function of φ) for an observer located at the Earth latitude $\ell_{\mathrm{site}} = -35.2°$ of the Pierre Auger Observatory.

the distortions induced by a dipole in the $\mathrm{d}N/\mathrm{d}\sin^2\theta$ distribution, we define $\Delta(\mathrm{d}N/\mathrm{d}\sin^2\theta)$ such that :

$$\Delta(\mathrm{d}N/\mathrm{d}\sin^2\theta) = \frac{1}{r}\left(\frac{\mathrm{d}N_{dipole}/\mathrm{d}\sin^2\theta - \mathrm{d}N_{iso}/\mathrm{d}\sin^2\theta}{\mathrm{d}N_{iso}/\mathrm{d}\sin^2\theta}\right). \tag{30}$$

Once multiplied by the dipole amplitude r, $\Delta(\mathrm{d}N/\mathrm{d}\sin^2\theta)$ gives directly the relative changes in the $\mathrm{d}N/\mathrm{d}\sin^2\theta$ distribution with respect to isotropy. Carrying out integrations over φ and α^0 yields to :

$$\Delta(\mathrm{d}N/\mathrm{d}\sin^2\theta) = \frac{N_{0,dipole}}{N_{0,iso}}\ \sin\ell_{\mathrm{site}}\sin\delta_d\cos\theta, \tag{31}$$

where both intensity normalisations $N_{0,iso}$ and $N_{0,dipole}$ are tuned to guarantee the same number of events observed in the covered region of the sky for each underlying angular distribution. This result is shown in the left panel of Fig. 12, for the latitude $\ell_{\mathrm{site}} = -35.2°$ of the Pierre Auger Observatory and for different dipole directions. Within the zenithal range $[0°, 55°]$ considered in this article, the relative changes - maximal for $\delta_d = \pm 90°$ - amount at most to $\simeq \pm 15\%$. So, even for an amplitude r as large as 10%, the relative changes in $\mathrm{d}N/\mathrm{d}\sin^2\theta$ would be within $\simeq \pm 1.5\%$, variation which - given the available statistics - is sufficiently low to be considered as negligible. Besides, the same calculation applied to the case of a symmetric quadrupolar anisotropy shows that the variation of $\Delta(\mathrm{d}N/\mathrm{d}\sin^2\theta)$ is less than $\simeq 0.1\%$, thus being negligible. Consequently, the distribution in $\mathrm{d}N/\mathrm{d}\sin^2\theta$ can be considered at first order as *insensitive* to large scale anisotropies, so that any significant deviation from a uniform distribution provides an empirical measurement of the zenithal dependence of the detection efficiency.

It is worth noting that the azimuthal distribution averaged over time is, on the other hand, sensitive to large scale anisotropies. Repeating the same calculation and integrating now over θ (in this example between 0 and 60°) and α^0 yields the $\Delta(\mathrm{d}N/\mathrm{d}\varphi)$ relative changes :

$$\Delta(\mathrm{d}N/\mathrm{d}\varphi) = \frac{N_{0,dipole}}{N_{0,iso}}\,\frac{\sin\delta_d\cos\ell_{\mathrm{site}}}{24}\,\bigg(7\tan(\ell_{\mathrm{site}}) + 3\sqrt{3}\sin(\varphi)\bigg). \tag{32}$$

This function is shown in the right panel of Fig. 12, for $\delta_d = 90°$ (dashed line) and $\delta_d = -90°$ (dotted line). The amplitude of the dipole wave is now $\simeq 0.5$. As well, the influence of a quadrupole on $\Delta(\mathrm{d}N/\mathrm{d}\varphi)$ is illustrated by the dashed-dotted line (oblate symmetric quadrupole in this example). Since, at the Earth latitude of the Pierre Auger Observatory, any genuine large scale pattern which depends on the declination translates into azimuthal modulations of the event rate *similar* to the ones induced by experimental effects, it is thus mandatory to model accurately the dependence on azimuth of the detection efficiency for disentangling local from celestial effects.

Appendix B : Modulation of the detection efficiency induced by a tilted array

To estimate the modulation of the detection efficiency induced by a tilted array, we consider here that in the absence of tilt, the corresponding detection efficiency function $\epsilon_{\mathrm{notilt}}$ depends *only* on the energy and the zenith angle and can be parameterised in a good approximation as :

$$\epsilon_{\mathrm{notilt}}(E,\theta) = \frac{E^3}{E^3 + E^3_{0.5}(\theta)}. \tag{33}$$

$E_{0.5}(\theta)$ is the zenithal-dependent energy at which $\epsilon_{\mathrm{notilt}}(E,\theta) = 0.5$. In case of a tilted array, this parameter depends also on the azimuth angle, which is then the source of the azimuthal modulation of the detection efficiency. To understand this, it is useful to consider for any given shower with parameters (E,θ,φ) the circle in the shower plane corresponding to the region in which a signal S larger than some specified threshold value S_0 is expected. Let $r_0(\zeta)$ denote the radius of this circle, ζ being the tilt angle of the SD array. The detection efficiency, and hence also the parameter $E_{0.5}$, is ultimately a function of the average number of detectors contained in the projection of this circle into the ground, given by :

$$\langle n_{\mathrm{det}}\rangle\,(S > S_0) \propto \frac{r_0^2}{h^2|\mathbf{n}_\perp\cdot\mathbf{n}|}, \tag{34}$$

where $h = 1.5$ km is the nominal separation between surface detectors. The radii $r_0(\zeta)$ obtained with the tilted array leading to the same value of $\langle n_{\mathrm{det}}\rangle$ can be related to $r_0(\zeta = 0)$ through :

$$r_0^2(\zeta) = r_0^2(\zeta = 0)\frac{|\mathbf{n}_\perp\cdot\mathbf{n}|}{\cos\theta}. \tag{35}$$

Hence, we can obtain the relation between the energies $E_{0.5}$ with tilt ($E_{0.5}^{\mathrm{tilt}}$) and without tilt ($E_{0.5}$) by comparing the cosmic ray energies required to get the value S_0 at radius $r_0(\zeta)$ and at radius $r_0(\zeta=0)$. Approximating the lateral distribution function of the signal near the radius r_0 as a power law $S(r) \propto Er^{-3}$, we obtain the following relation :

$$E_{0.5}^{\mathrm{tilt}}(\theta,\varphi) = E_{0.5}(\theta)\left(\frac{r_0(\zeta)}{r_0(\zeta=0)}\right)^3 \simeq E_{0.5}(\theta)[1+\zeta\tan\theta\cos{(\varphi-\varphi_0)}]^3. \quad (36)$$

Then, subtracting $\epsilon_{\mathrm{notilt}}$ to ϵ_{tilt} leads to Eqn. 9.

Appendix C : Determination of upper limits on dipole amplitudes

To determine upper limits on the dipole amplitudes, Linsley described the procedure to follow in the case of first harmonic analysis in right ascension (Linsley 1975). We adapt here this procedure to the case of the dipolar reconstruction adopted in section 5.2.

Here, the data set is supposed to have been drawn at random from an underlying dipolar distribution characterised by $\mathbf{d}$, whose value is unknown. In the limit of large number of events, the joint p.d.f. $p_{D_X,D_Y,D_Z}(\overline{d}_x,\overline{d}_y,\overline{d}_z)$ can be factorised in terms of three Gaussian distributions $N(\overline{d}_i-d_i,\sigma_i)$:

$$p_{D_X,D_Y,D_Z}(\overline{d}_x,\overline{d}_y,\overline{d}_z;d_x,d_y,d_z) = N(\overline{d}_x-d_x,\sigma)N(\overline{d}_y-d_y,\sigma)N(\overline{d}_z-d_z,\sigma_z). \quad (37)$$

The joint p.d.f. $p_{R,\Delta,A}(\overline{r},\overline{\delta},\overline{\alpha})$ expressing the dipole components in spherical coordinates is then obtained by performing the Jacobian transformation :

$$\begin{aligned} p_{R,\Delta,A}(\overline{r},\overline{\delta},\overline{\alpha};d,\delta_d,\alpha_d) &= \left|\frac{\partial(\overline{d}_x,\overline{d}_y,\overline{d}_z)}{\partial(\overline{r},\overline{\delta},\overline{\alpha})}\right| p_{D_X,D_Y,D_Z}(\overline{d}_x(\overline{r},\overline{\delta},\overline{\alpha}),\overline{d}_y(\overline{r},\overline{\delta},\overline{\alpha}),\overline{d}_z(\overline{r},\overline{\delta},\overline{\alpha})) \\ &= \frac{\overline{r}^2\cos\overline{\delta}}{(2\pi)^{3/2}\sigma^2\sigma_z}\exp\left[-\frac{(\overline{r}\sin\overline{\delta}-d\sin\delta_d)^2}{2\sigma_z^2}\right] \\ &\times \exp\left[-\frac{(\overline{r}\cos\overline{\delta}\cos\overline{\alpha}-d\cos\delta_d\cos\alpha_d)^2}{2\sigma^2}\right] \\ &\times \exp\left[-\frac{(\overline{r}\cos\overline{\delta}\sin\overline{\alpha}-d\cos\delta_d\sin\alpha_d)^2}{2\sigma^2}\right]. \end{aligned} \quad (38)$$

Each analysed data set having been selected at random from an ensemble in which all possible values of $\mathbf{d}$ are equally represented, the various d, δ_d and α_d combinations have relative probability $p_{R,\Delta,A}(\overline{r},\overline{\delta},\overline{\alpha};d,\delta_d,\alpha_d)/p_{R,\Delta,A}(\overline{r},\overline{\delta},\overline{\alpha};d=0)$. This allows us to define the joint p.d.f. $\tilde{p}_{R,\Delta,A}$ by requiring this ratio to be normalised to unity :

$$\tilde{p}_{R,\Delta,A}(\overline{r},\overline{\delta},\overline{\alpha};d,\delta_d,\alpha_d) = K(r,\delta)\ \exp\left[\frac{\overline{r}d\cos\overline{\delta}\cos\delta_d\cos{(\overline{\alpha}-\alpha_d)}}{\sigma^2}\right]$$

$$\times \quad \exp\left[\frac{\overline{r}d\sin\overline{\delta}\sin\delta_d}{\sigma_z^2} - \frac{d^2\cos^2\delta_d}{2\sigma^2} - \frac{d^2\sin^2\delta_d}{2\sigma_z^2}\right], \tag{39}$$

where the normalisation reads :

$$\begin{aligned} K(r,\delta) &= 2\pi\ I_0\left(\frac{\overline{r}d\cos\overline{\delta}\cos\delta_d}{\sigma^2}\right) \\ &\times \int \mathrm{d}d\ \mathrm{d}\delta_d\ \exp\left[-\frac{d^2\cos^2\delta_d}{2\sigma^2} - \frac{d^2\sin^2\delta_d}{2\sigma_z^2} + \frac{\overline{r}d\sin\overline{\delta}\sin\delta_d}{\sigma_z^2}\right]. \end{aligned} \tag{40}$$

I_0 is here the modified Bessel function of the first kind with order 0. Integration of $\tilde{p}_{R,\Delta,A}$ over δ_d and α_d yields the $\tilde{p}_R$ p.d.f., from which upper limits on d can be obtained within a confidence level $C.L.$ by inverting the relation :

$$\int_{\overline{r}_{data}}^{1} \mathrm{d}\overline{r}\ \tilde{p}_R(\overline{r},\overline{\delta};d^{UL}) = C.L. \tag{41}$$

Due to the non-uniform directional exposure in declination, the resulting upper limits actually depend on the declination through the dependence of $\tilde{p}_R$ on $\overline{\delta}$. In practice, this dependence is small, which is why we presented in section 7 upper limits *averaged* over the declination.

Appendix D : Determination of upper limits on quadrupole amplitudes

To determine upper limits on quadrupole amplitudes, we rely on Monte-Carlo simulations. For each possible amplitude λ_+ (β), we estimate the p.d.f. $p_{\Lambda_+}(\overline{\lambda}_+;\lambda_+)$ ($p_B(\overline{\beta};\beta)$) with a given number of events N and a given exposure $\tilde{\omega}$. The amplitude λ_+^{UL} such that $\int_{\overline{\lambda}_{+,data}}^{\infty} \mathrm{d}\overline{\lambda}_+\ \tilde{p}_\Lambda(\overline{\lambda}_+;\lambda_+^{UL}) = C.L.$ is a relevant upper limit (and respectively for β^{UL}).

Alternatively to the previous procedure used to derive upper limits on dipole amplitudes, this procedure can lead to upper limits tighter than the upper bounds for isotropy $\overline{\lambda}_{+,99}$ when the measured values of $\overline{\lambda}_{+,data}$ are smaller than the expected average for isotropy. To cope with this undesired behaviour, the upper limits presented in section 7 are defined as $\max(\overline{\lambda}_{+,99},\lambda_+^{UL})$.

REFERENCES

R. U. Abbasi *et al.* (The IceCube Collaboration), ApJ 718 (2010) 194

A. A. Abdo *et al.* (The Milagro Collaboration), ApJ 698 (2009) 2121

M. Aglietta *et al.* (The EAS-TOP Collaboration), ApJL 692 (2009) L130-L133

M. Amenomori *et al.* (The Tibet ASγ Collaboration), Science 314 (2006) 439

R. Beck, Space Sci. Rev. 99, 243 (2001)

V. S. Berezinsky, S. I. Grigorieva, B. I. Hnatyk, Astropart. Phys. 21 (2004) 617625

V. S. Berezinsky, A. Z. Gazizov, S. I. Grigorieva, Phys. Rev. D 74 (2006) 043005

P. Billoir, O. Deligny, JCAP 02 (2008) 009

D. J. Bird *et al.*, (Fly's Eye Collaboration), Phys. Rev. Lett. 71 (1993) 3401

G. R. Blumenthal, Phys. Rev. D1 (1970) 1596

C. Bonifazi, A. Letessier-Selvon, E.M. Santos, Astropart. Phys. 28 (2008) 523

C. Bonifazi for the Pierre Auger Collaboration, Nucl. Phys. Proc. Suppl. 190 (2009) 20

A. Calvez, A. Kusenko, S. Nagataki, Phys. Rev. Lett. 105 (2010) 091101

J. Candia, S. Mollerach, E. Roulet, JCAP 0305 (2003) 003

A. H. Compton, I. A. Getting, Phys. Rev. 47 (1935) 817

D. Cutler, D. Groom, Nature 322 (1986) 434

D. Eichler, M. Pohl, ApJ 742 (2011) 114

R. Engel for the Pierre Auger Collaboration, Proceedings of the 30th ICRC, Mérida, 2007

G. Farrar, R. Jansson, arXiv:1204.3662, submitted to ApJ

G. Giacinti *et al.*, arXiv:1112.5599, submitted to JCAP

D. Harari, S. Mollerach, E. Roulet, JCAP 11 (2010) 033

A. M. Hillas, Phys. Lett. 24A 677 (1967)

M. Kachelriess, P. Serpico, Phys. Lett. B 640 (2006) 225-229

M. A. Lawrence, R. J. O. Reid, A. A. Watson, J. Phys. G 17 (1991) 733

T.-P. Li, Y.-Q. Ma, ApJ 272 (1983) 317

J. Linsley, Proceedings of the 8th ICRC, Jaipur, vol. 4, 1963, p. 77

J. Linsley, Phys. Rev. Lett. 34 (1975) 221101

H. J. Mathes for the Pierre Auger Collaboration, Proceedings of the 32nd ICRC, Beijing, 2011

M. Nagano *et al.*, J. Phys. G 18 (1992) 423

R. Pesce for the Pierre Auger Collaboration, Proceedings of the 32nd ICRC, Beijing, 2011

The Pierre Auger Collaboration, Nucl. Instr. and Meth. A 523 (2004) 50

The Pierre Auger Collaboration, Phys. Rev. Lett. 101 (2008) 061101

The Pierre Auger Collaboration, Astropart. Phys. 32 (2009) 89

The Pierre Auger Collaboration, Phys. Lett. B 685 (2010a) 239

The Pierre Auger Collaboration, Nucl. Instr. and Meth. A 613 (2010b) 29

The Pierre Auger Collaboration, Phys. Rev. Lett. 104 (2010c) 091101

The Pierre Auger Collaboration, Astropart. Phys. 34 (2011a) 627-639

The Pierre Auger Collaboration, JCAP 11 (2011b) 022

The Pierre Auger Collaboration, in preparation (2012a)

The Pierre Auger Collaboration, submitted to ApJ (2012b)

M. S. Pshirkov *et al.*, ApJ 738 (2011) 192

V. Ptuskin *et al.*, Astron. Astrophys. 268 (1993) 726

F. Sanchez for the Pierre Auger Collaboration, Proceedings of the 32nd ICRC, Beijing, 2011

P. Sommers, Astropart. Phys. 14 (2001) 71

K. O. Thielheim, W. Langhoff, J. Phys. A, 694 (1968)

V. N. Zirakashvili *et al.*, AstL. 24 (1998) 139

This manuscript was prepared with the AAS LaTeX macros v5.2.